MODEL ORDER REDUCTION OF HÆMODYNAMICS BY SPACE—TIME REDUCED BASIS AND REDUCED FLUID—STRUCTURE INTERACTION

Riccardo Tenderini

Institute of Mathematics Ècole Polytechnique Fédérale de Lausanne (EPFL) CH–1015 Lausanne, Switzerland

Simone Deparis

Institute of Mathematics Ècole Polytechnique Fédérale de Lausanne (EPFL) CH–1015 Lausanne, Switzerland

ABSTRACT

In this work, we apply the space-time Galerkin reduced basis (ST-GRB) method to a reduced fluid-structure interaction model, for the numerical simulation of hæmodynamics in arteries. In essence, ST-GRB extends the classical reduced basis (RB) method, exploiting a data-driven lowdimensional linear encoding of the temporal dynamics to further cut the computational costs. The current investigation brings forth two key enhancements, compared to previous works on the topic. On the one side, we model blood flow through the Navier-Stokes equations, hence accounting for convection. In this regard, we implement a hyper-reduction scheme, based on approximate spacetime reduced affine decompositions, to deal with nonlinearities effectively. On the other side, we move beyond the constraint of modelling blood vessels as rigid structures, acknowledging the importance of elasticity for the accurate simulation of complex blood flow patterns. To limit computational complexity, we adopt the Coupled Momentum model, incorporating the effect of wall compliance in the fluid's equations through a generalized Robin boundary condition. In particular, we propose an efficient strategy for handling the spatio-temporal projection of the structural displacement, which ultimately configures as a by-product. The performances of ST-GRB are assessed in three different numerical experiments. The results confirm that the proposed approach can outperform the classical RB method, yielding precise approximations of high-fidelity solutions at more convenient costs. However, the computational gains of ST-GRB vanish if the number of retained temporal modes is too large, which occurs either when complex dynamics arise or if very precise solutions are sought.

Keywords Reduced order modeling, Space–time reduced basis, Navier–Stokes equations, Hæmodynamics, Fluid–structure interaction

1 Introduction

The use of physics—based computational models for the cardiovascular system has significantly grown in recent years, enabling the accurate simulation of hæmodynamics, tissue mechanics, and of the cardiovascular system in general. As a matter of fact, these predictive models, originally designed for surgical planning, now serve purposes well beyond their initial application, thanks to their ability to combine clinical data with physical knowledge of the processes underlying the cardiac function [1, 2]. High–fidelity personalized numerical simulations of hæmodynamics can yield exceptionally accurate descriptions of the blood flow conditions by leveraging state—of—the—art computational fluid dynamics (CFD) techniques. Nevertheless, they require important computational resources and entail large computing times, which hinders their effective use in the daily clinical practice. As a way to mitigate this issue, Reduced Order Models (ROMs) allow to conduct simulations on standard consumer devices with computational times of the order of minutes or even seconds, hence representing a cost—effective alternative to the classical CFD approaches. Such substantial performance improvements come at the cost of accuracy losses, that remain nonetheless within the range of acceptability for many applications. Therefore, ROMs can be particularly useful in many—query scenarios, namely in cases where multiple simulations have to be carried out, considering different values of some parameters,

related to the system properties. Uncertainty Quantification (UQ) is perhaps the most relevant example in this sense [3].

In hæmodynamics, ROMs can be roughly subdivided into three categories: physics-based — such as OD, 1D models [4] — projection-based — such as the Reduced Basis (RB) method [5] — and data-driven [6]. Hybrid approaches are also possible; for instance, several methods combining data availability with knowledge of the underlying physical laws — such as Physics-Informed Neural Networks [7, 6, 8] — have been introduced over the last decade. We refer to [1, 9] for comprehensive literature reviews of the topic. In this work, we focus on projection-based ROMs, and more precisely on the RB method. The latter stems from the orthogonal projection (in space) of the model equations onto linear subspaces, generated through Proper Orthogonal Decomposition (POD) from a database of high-fidelity solutions. Despite having been originally conceived for steady problems, the RB method can be seamlessly extended to time-dependent ones. This leads to the time integration of low-dimensional systems of ODEs, which is usually performed with the same scheme and timestep size used for the full-order model (FOM) [10]. In many cases, the dimensionality reduction in space introduced by the RB method is enough to drastically cut the computational costs. Indeed, the FOM spatial complexity typically exceeds the temporal one by a few orders of magnitude. However, in problems where either the simulation interval should be very large or the timestep size should be very small in order to capture some relevant physical behaviours, temporal complexity does represent a bottleneck and valuable computational gains may be difficult to realize with classical approaches.

To overcome the temporal complexity bottleneck, in this work we consider Space-Time Reduced Basis (ST-RB) methods [11, 12, 13, 14, 15, 16, 17, 18, 19]. In [18], we already investigated the use of ST-RB methods based on spatio-temporal (Petrov-)Galerkin projections for hæmodynamics. In particular, we proposed two stabilization procedures, that guarantee the well-posedness of the resulting low-dimensional problem. Both approaches attained remarkable computational gains compared to the baseline RB method and accuracies matching the theoretical expectations. However, these results were obtained in a simplified setting, where we neglected the presence of the nonlinear convective term in the momentum conservation equation (Stokes equations) and modelled arterial walls as rigid structures, via the imposition of no-slip boundary conditions. Solely focusing on the case of a Galerkin projection in space-time, the current investigation brings forth two key enhancements. On the one hand, we model blood flow by the unsteady incompressible Navier-Stokes equations, recognizing the primary importance of convection for the precise simulation of hæmodynamics. On the other hand, we move beyond the no-slip constraint, taking wall compliance into account for the accurate approximation of complex blood flow patterns [20, 21, 22]. In principle, this would imply solving a fluid-structure interaction (FSI) problem, where the Navier-Stokes equations in a moving domain are coupled with elasto-mechanical models that describe structural displacements, by means of an Arbitrary Lagrangian-Eulerian (ALE) approach. Even if the development of efficient parallel algorithms [23, 24] and of ad hoc preconditioning strategies [25, 26] led to significant efficiency improvements, the computational cost of FSI simulations remains nonetheless high. In the hæmodynamics context, this poses limitations to their application in the standard clinical practice and in particular to their use for real-time diagnoses. To mitigate this issue, we consider a reduced FSI model, called Coupled Momentum, originally proposed in [27] and successively further investigated e.g. in [28, 29]. Under the hypothesis of small deformations — reasonable in the majority of large blood vessels the coupled momentum model assumes that the fluid domain is fixed and incorporates the effect of wall compliance on the blood flow within the Navier-Stokes equations, by means of a generalized Robin boundary condition. Furthermore, compared to [18], we impose absorbing resistance boundary conditions at the outlets, enforcing a linear relationship between pressure and volumetric flow rate. An appropriate choice of the outlet boundary conditions, able to adequately model the effect of the downstream vasculature, is important for performing accurate personalized simulations, and it becomes fundamental when accounting for compliant vessel walls. In particular, well-calibrated physiological boundary conditions prevent spurious reflecting pressure waves to appear, thus smoothing the overall problem dynamics and enhancing the computational gains of model order reduction in space-time.

The manuscript is structured as follows. In Section 2, we introduce the unsteady incompressible Navier–Stokes equations and the coupled momentum model, and we discuss their weak formulation and high–fidelity discretization by the Finite Element (FE) method. In Section 3, we describe the application of the ST–RB method based on a Galerkin projection to the problem at hand, detailing the assembling of the reduced convective term, the treatment of the generalized Robin boundary condition and the handling of non–zero initial conditions. In Section 4, we present three different numerical tests (two idealized and one physiological) to empirically assess the method performances. Finally, in Section 5, we summarize the main findings of the work and envision potential further developments.

2 Model order reduction of FSI: the Coupled Momentum model

2.1 Physical problem

In sufficiently large vessels, blood can be approximated as a Newtonian fluid and its flow can be modelled by the incompressible Navier–Stokes equations [30]. Let $\Omega \subset \mathbb{R}^3$ be an open, simply connected and bounded domain and let $\partial\Omega$ be its boundary. Let [0,T], with T>0, be the time interval of interest. Then, the unsteady incompressible Navier–Stokes equations read as follows:

$$\begin{cases} \rho_f \underline{u}_t + \rho_f(\underline{u} \cdot \nabla)\underline{u} - \nabla \cdot (2\mu_f \nabla^s \underline{u}) + \nabla p = \underline{0} & \text{in } \Omega \times (0, T] ,\\ \nabla \cdot \underline{u} = 0 & \text{in } \Omega \times (0, T] . \end{cases}$$

$$(2.1)$$

Here $\underline{u}:\Omega\times(0,T]\to\mathbb{R}^3$ and $p:\Omega\times(0,T]\to\mathbb{R}$ denote velocity and pressure, respectively; \underline{u}_t is the partial derivative of the velocity with respect to time; $\rho_f,\mu_f\in\mathbb{R}^+$ are the blood density and viscosity, respectively; $\nabla^s\underline{u}=(\nabla\underline{u}+\nabla^T\underline{u})$ / 2 is the strain rate tensor. We remark that the first equation in Eq.(2.1), that enforces momentum conservation, is nonlinear, due to presence of the convective term $\underline{c}(\underline{u}):=\rho_f(\underline{u}\cdot\nabla)\underline{u}$. Eq.(2.1) must be endowed with suitable initial and boundary conditions to guarantee well–posedness. Since the velocity partial derivative in time appears, the initial condition is

$$\underline{u} = \underline{u}_0 \quad \text{in} \quad \Omega \times \{0\} \; ,$$

where $\underline{u}_0:\Omega\to\mathbb{R}^3$ is a prescribed velocity field at t=0. For the purpose of defining the boundary conditions, let $\{\Gamma,\Gamma_{\mathrm{IN}},\Gamma_{\mathrm{OUT}}\}$ be a partition of $\partial\Omega$, where Γ denotes the vessel wall and $\Gamma_{\mathrm{IN}},\Gamma_{\mathrm{OUT}}$ encode the ensemble of the inlet and outlet boundaries, respectively. In this work, we always prescribe velocity profiles at the inlets, whereas the nature of the outlet boundary conditions depends on the test case at hand. For this reason, we introduce $\Gamma_{\mathrm{D}}=\bigcup_{k=1}^{N_D}\Gamma_{\mathrm{D}}^k$ as the union of the N_D inlet/outlet boundaries where velocity profiles are enforced (Dirichlet boundaries); analogously, we define $\Gamma_{\mathrm{N}}:=\bigcup_{k=1}^{N_N}\Gamma_{\mathrm{N}}^k$ (Neumann boundaries) and $\Gamma_{\mathrm{R}}:=\bigcup_{k=1}^{N_R}\Gamma_{\mathrm{R}}^k$ (resistance boundaries). Clearly, it holds that $\Gamma_{\mathrm{IN}}\cup\Gamma_{\mathrm{OUT}}=\Gamma_{\mathrm{D}}\cup\Gamma_{\mathrm{N}}\cup\Gamma_{\mathrm{R}}$. Then, the inlet/outlet boundary conditions read as follows:

$$\begin{cases} \underline{u} = \underline{g}^k & \text{on } \Gamma_{\mathrm{D}}^k \times (0,T] \;, \; \; k = 1, \cdots, N_D \;; \\ \sigma(\underline{u},p) \; \underline{n} = \underline{0} & \text{on } \Gamma_{\mathrm{N}} \times (0,T] \;; \\ \sigma(\underline{u},p) \; \underline{n} + (R^{k'}Q^{k'}) \; \underline{n} = \underline{0} & \text{on } \Gamma_{\mathrm{R}}^{k'} \times (0,T] \;, \; \; k' = 1, \cdots, N_R \;; \end{cases}$$

where $\underline{g}^k:\Gamma^k_{\mathrm{D}}\times(0,T]\to\mathbb{R}^3$ is the Dirichlet boundary datum on $\Gamma^k_{\mathrm{D}},\,\sigma(\underline{u},p)=2\mu_f\nabla^s\underline{u}-pI$ is the Cauchy stress tensor, $\underline{n}=\underline{n}(\underline{x})$ is the outward unit normal vector to $\partial\Omega$ at \underline{x} , and $Q^{k'}=\int_{\Gamma^{k'}_{\mathrm{B}}}\underline{u}\cdot\underline{n}$ is the volumetric flow rate at $\Gamma^{k'}_{\mathrm{R}}$.

To limit computational complexity, whilst taking into account the effect of the vessel wall compliance on blood flow, we employ the *Coupled Momentum* model [27]. To this aim, we consider a pseudo–compressible, linear elastic, isotropic, homogeneous material for the vessel structure and we suppose to work under a small deformations hypothesis. In this setting, by approximating the three–dimensional vessel structure as a thin elastic membrane, the coupled momentum model translates the wall mechanics into an *ad hoc* generalized Robin boundary condition, enforced on Γ . Let $\rho_s \in \mathbb{R}^+$ be the structure density and let $\underline{d}: \Gamma \times (0,T] \to \mathbb{R}^3$ denote the membrane displacement. Following [31], we consider a membrane model in the plane stress configuration with an augmented shear stress in the transverse directions. This leads to the following linear stress–strain relation:

$$\Pi_{\Gamma}(\underline{d}) = h_s \Big(\lambda_1 (\nabla_{\Gamma} \cdot \underline{d}) \left(I - \underline{n} \otimes \underline{n} \right) + 2\lambda_2 \nabla_{\Gamma}^s (\underline{d}) + 2\lambda_2 (\gamma_{sh} - 1) \nabla_{\Gamma}^s (\underline{d}) \, \underline{n} \otimes \underline{n} \Big) , \qquad (2.2)$$

where $\nabla_{\Gamma}:\mathbb{R}^3 \to \mathbb{R}^{3 \times 3}$ is the surface gradient operator on Γ , i.e. $\nabla_{\Gamma}(\underline{d}) := \nabla \underline{d} \ (I - \underline{n} \otimes \underline{n})$, and $\nabla^s_{\Gamma}(\underline{d})$ denotes its symmetric part; the symbol \otimes denotes the tensor product and $I \in \mathbb{R}^{3 \times 3}$ is the identity matrix. The quantity $h_s \in \mathbb{R}^+$ represents the membrane thickness, $\gamma_{sh} = 5/6$ is the transverse shear coefficient, while $\lambda_1, \lambda_2 \in \mathbb{R}$ are parameters whose expressions depend on the Young modulus E and on the Poisson ratio ν of the material:

$$\lambda_1 = \frac{E\nu}{(1+\nu)(1-\nu)} \;, \qquad \lambda_2 = \frac{E}{2(1+\nu)} \;.$$

Furthermore, as done in [32], we optionally take into account the elastic response of the surrounding tissues, to avoid non–physiological rigid vessel motions [33]. We refer the reader to [28] for further details on the coupled momentum model and on its relevance in the context of hæmodynamics.

Remark 2.1 For simplicity, in the following we restrict to homogeneous initial conditions for both velocity and displacement. The full-order and reduced-order problem formulations with non-zero initial conditions are detailed in Appendix A.

2.2 Full-order algebraic formulation

We are interested in deriving a high-fidelity space-time algebraic formulation of the problem at hand. Concerning the spatial discretization, we employ the FE method and consider a stable couple $(\mathcal{V}_h, \mathcal{Q}_h)$ of FE spaces for velocity and pressure, built on a tetrahedralization of Ω . We remark that $(\mathcal{V}_h, \mathcal{Q}_h)$ must satisfy the *inf-sup* condition, in order to guarantee the well-posedness of the discrete problem [34, 35]. For the temporal discretization, we partition the time interval [0,T], by defining discrete time instants $\{t_n\}_{n=0}^{N^t}$ such that $t_n=n\Delta t$; $\Delta t\in\mathbb{R}^+$ is called the timestep size. To integrate the multidimensional ODE stemming from the application of the FE method, we rely on implicit BDF schemes. So, given a generic vector quantity $\phi=\phi(\cdot,t)$, we approximate its first-order partial derivative in time as

$$\left. \frac{\partial \phi}{\partial t} \right|_{t=t_{n+1}} = \frac{1}{\beta \Delta t} \left(\phi_{n+1} - \sum_{s=1}^{S} \alpha_s \phi_{n+1-s} \right) \qquad \text{with} \quad \phi_m = \phi(\cdot, t_m) \;,$$

for suitably defined coefficients $\alpha_1, \ldots, \alpha_S, \beta \in \mathbb{R}$. Additionally, we impose the inhomogeneous Dirichlet boundary conditions on Γ_D with Lagrange multipliers, to facilitate the extension of the proposed approach for coupling several subdomains [36]. To this aim, we introduce the (discrete) space of Lagrange multipliers $\mathcal{L}_h = \prod_{k=1}^{N_D} \mathcal{L}_h^k$. We refer to [36] for further details on the choice of the space of Lagrange multipliers and on its discretization; we refer to [18] for a discussion on the well–posedness of the resulting problem, that exhibits a twofold saddle–point structure. Ultimately, the following finite–dimensional approximations of velocity, pressure and Lagrange multipliers are considered:

$$\underline{u}_h(\underline{x},t) = \sum_{i=1}^{N_u^s} u_i(t) \ \underline{\varphi}_i^u(\underline{x}) \in \mathcal{V}_h \ ; \qquad p_h(\underline{x},t) = \sum_{i=1}^{N_p^s} p_i(t) \ \varphi_i^p(\underline{x}) \in \mathcal{Q}_h \ ; \qquad \underline{\lambda}_h^k(\underline{x},t) = \sum_{i=1}^{N_h^k} \boldsymbol{\lambda}_i^k(t) \ \underline{\eta}_i^k(\underline{x}) \in \mathcal{L}_h^k \ ;$$

where $N_u^s := \dim(\mathcal{V}_h)$, $N_p^s := \dim(\mathcal{P}_h)$, $N_\lambda^k := \dim(\mathcal{L}_h^k)$, for $k = 1, \dots, N_D$. Also, we define $N_\lambda := \prod_{k=1}^{N_d} N_\lambda^k$. The time-dependent vectors $\boldsymbol{u} \in \mathbb{R}^{N_u^s}$, $\boldsymbol{p} \in \mathbb{R}^{N_p^s}$, $\boldsymbol{\lambda^k} \in \mathbb{R}^{N_\lambda^k}$ collect the velocity, pressure and Lagrange multipliers Degrees of Freedom (DOFs).

In view of the use of model order reduction techniques, we introduce a parametrization in the problem. Firstly, we parametrize the inflow/outflow rates at the Dirichlet boundaries. For every $k \in \{1, \dots N_D\}$, we assume that the Dirichlet datum g^k on Γ^k_D can be factorized as

$$\underline{g}^{k}(\underline{x}, t; \boldsymbol{\mu_{f}}) := \underline{g}_{k}^{s}(\underline{x}) g_{k}^{t}(t; \boldsymbol{\mu_{f}}) \qquad (\underline{x}, t) \in \Gamma_{D}^{k} \times (0, T],$$

$$(2.3)$$

where $\mu_f \in \mathcal{P}_f \subset \mathbb{R}^{N_\mu^f}$ is a vector collecting parameters associated to the prescribed volumetric flow rates. Secondly, we introduce a source of parametrization that affects the vessel structure mechanics. To this aim, we define the parameter vector $\mu_m := [h_s, \rho_s, E, \nu] \in \mathcal{P}_m \subset \mathbb{R}^{N_\mu^m}$, where $N_\mu^m = 4$; the entries of μ_m have been defined in Section 2.1. We remark that, since the stress–strain relation reported in Eq.(2.2) is linear with respect to $\lambda_1(E, \nu)$, $\lambda_2(E, \nu)$, the considered parametrization is affine. The coefficients that multiply the affine components are stored in the vector $\tilde{\mu}_m := [h_s \rho_s, h_s \lambda_1(E, \nu), 2h_s \lambda_2(E, \nu)] \in \mathbb{R}^{N_\mu^m-1}$.

We can now introduce the following FOM matrices and vectors:

$$\begin{split} \boldsymbol{A} &\in \mathbb{R}^{N_u^s \times N_u^s}: & \boldsymbol{A}_{ij} = 2\mu_f \int_{\Omega} \nabla^s(\underline{\varphi}_j^u) : \nabla^s(\underline{\varphi}_i^u) \; ; & \boldsymbol{M} &\in \mathbb{R}^{N_u^s \times N_u^s}: & \boldsymbol{M}_{ij} = \rho_f \int_{\Omega} \underline{\varphi}_j^u \cdot \underline{\varphi}_i^u \; ; \\ \boldsymbol{B} &\in \mathbb{R}^{N_p^s \times N_u^s}: & \boldsymbol{B}_{ij} = -\int_{\Omega} \varphi_i^p \; \nabla \cdot \underline{\varphi}_j^u \; ; & \boldsymbol{L}^k &\in \mathbb{R}^{N_\lambda^k \times N_u^s}: & \boldsymbol{L}^k_{ij} = \int_{\Gamma_D} \underline{\eta}_i^k \cdot \underline{\varphi}_j^u \; ; \\ \boldsymbol{M}_{\boldsymbol{s}} &\in \mathbb{R}^{N_u^s \times N_u^s}: & (\boldsymbol{M}_{\boldsymbol{s}})_{ij} = \int_{\Gamma} \underline{\varphi}_j^u \cdot \underline{\varphi}_i^u \; ; & \boldsymbol{A}_{\boldsymbol{s}}^q &\in \mathbb{R}^{N_u^s \times N_u^s}: & (\boldsymbol{A}_{\boldsymbol{s}}^q)_{ij} = a_{mem}^q(\underline{\varphi}_j^u ; \underline{\varphi}_i^u) \; ; \\ \boldsymbol{c}(\underline{u}_h) &\in \mathbb{R}^{N_u^s}: & \boldsymbol{c}(\underline{u}_h)_i = \int_{\Omega} \rho_f \left((\underline{u}_h \cdot \nabla) \, \underline{\varphi}_j^u \right) \cdot \underline{\varphi}_i^u \; ; & \boldsymbol{g}_k^s &\in \mathbb{R}^{N_\lambda^k}: & (\boldsymbol{g}_k^s)_i = \int_{\Gamma_D^k} \underline{g}_k^s \cdot \underline{\eta}_i^k \; ; \\ \boldsymbol{q}^{k'} &\in \mathbb{R}^{N_u^s}: & (\boldsymbol{q}^{k'})_i = \int_{\Gamma_D^{k'}} \underline{\varphi}_i^u \cdot \underline{n} \; ; & \boldsymbol{R}^{k'} &\in \mathbb{R}^{N_u^s \times N_u^s}: & (\boldsymbol{R}^{k'})_{ij} = R^{k'} (\boldsymbol{q}^{k'})_i \; (\boldsymbol{q}^{k'})_j \; ; \end{split}$$

where $k=1,\cdots,N_D,\,k'=1,\cdots,N_R$, and q=1,2. The function $\underline{g}_h^k\in\mathcal{V}_h$ is the finite element approximation of $\underline{g}_k^s\in L^2(\Gamma_D^k)$ introduced in Eq.(2.3), while the following bilinear forms are considered for the assembling of the

matrices $\{A_s^q\}_{q=1}^2$:

$$a_{mem}^{1}\left(\underline{\varphi}_{j}^{u};\underline{\varphi}_{i}^{u}\right) = \beta \Delta t \int_{\Gamma} \left(\nabla_{\Gamma} \cdot \underline{\varphi}_{j}^{u}\right) \left(I - \underline{n} \otimes \underline{n}\right) : \nabla_{\Gamma}\underline{\varphi}_{i}^{u} ;$$

$$a_{mem}^{2}\left(\underline{\varphi}_{j}^{u};\underline{\varphi}_{i}^{u}\right) = \beta \Delta t \int_{\Gamma} \nabla_{\Gamma}^{s}\underline{\varphi}_{j}^{u} : \nabla_{\Gamma}\underline{\varphi}_{i}^{u} + (\gamma_{sh} - 1) \left(\nabla_{\Gamma}^{s}\underline{\varphi}_{j}^{u}\underline{n} \otimes \underline{n}\right) : \nabla_{\Gamma}\underline{\varphi}_{i}^{u} .$$

To ease the notation, we aggregate the information relative to the Lagrange multipliers by introducing

$$\boldsymbol{L} = \left[\left(\boldsymbol{L}^1 \right)^T | \cdots | \left(\boldsymbol{L}^{N_D} \right)^T \right]^T \\ \in \mathbb{R}^{N_{\lambda} \times N_u^s}; \qquad \boldsymbol{g}(t; \boldsymbol{\mu_f}) = \left[\left(\boldsymbol{g}_1^s \right)^T g_1^t(t; \boldsymbol{\mu_f}) | \cdots | \left(\boldsymbol{g}_{N_D}^s \right)^T g_{N_D}^t(t; \boldsymbol{\mu_f}) \right]^T \\ \in \mathbb{R}^{N_{\lambda}}.$$

and we define the following cumulative resistance matrix:

$$oldsymbol{R} = \sum_{k'=1}^{N_R} oldsymbol{R}^{k'} \ \in \mathbb{R}^{N_u^s imes N_u^s} \ .$$

Let $\boldsymbol{w}_n := [\boldsymbol{u}_n, \boldsymbol{p}_n, \boldsymbol{\lambda}_n]^T \in \mathbb{R}^{N^s}$ be the discrete solution at time t_n , with $N^s := N_u^s + N_p^s + N_\lambda$; let $\boldsymbol{d}_n \in \mathbb{R}^{N_u^s}$ be the discrete representation of the displacement at time t_n , expressed with respect to trace of the velocity basis functions on Γ . Furthermore, let us define $\boldsymbol{c}(\boldsymbol{u}_n) := \boldsymbol{c} \big(\sum_k \boldsymbol{u}_{n,k} \underline{\varphi}_k^u \big) \in \mathbb{R}^{N_u^s}$. Then, given \boldsymbol{w}_{n+1-s} for $s=1,\cdots,S$, the solution \boldsymbol{w}_{n+1} at time t_{n+1} is such that:

$$r(\mathbf{w}_{n+1}) := H\mathbf{w}_{n+1} - \sum_{s=1}^{S} \alpha_s H\mathbf{w}_{n+1-s} - \beta \Delta t F(t_{n+1}, \mathbf{w}_{n+1}, \mathbf{d}_{n+1}) = \mathbf{0},$$
 (2.4)

where
$$m{H}m{w}_n = \left[\left(\left. \left(m{M} + (ilde{m{\mu}}_{m{m}})_1 \; m{M}_{m{s}}
ight) m{u}_n
ight)^T, \; m{0}_{N_p^s}{}^T, \; m{0}_{N_\lambda}{}^T
ight]^T$$
 and

$$egin{aligned} oldsymbol{F}(t_n, oldsymbol{w}_n, oldsymbol{d}_n) &= egin{bmatrix} oldsymbol{0} \ oldsymbol{0} \ oldsymbol{q}(t_n; oldsymbol{\mu}_{oldsymbol{f}}) \end{bmatrix} - egin{bmatrix} oldsymbol{A} + oldsymbol{R} & oldsymbol{B}^T & oldsymbol{L}^T \ oldsymbol{B} & oldsymbol{0} & oldsymbol{0} \ oldsymbol{L} & oldsymbol{0} & oldsymbol{0} \end{bmatrix} - egin{bmatrix} oldsymbol{C}(oldsymbol{u}_n) + oldsymbol{c}_n oldsymbol{M}_n) & oldsymbol{d}_n \ oldsymbol{0} & oldsymbol{0} \end{bmatrix} - egin{bmatrix} oldsymbol{A} oldsymbol{s}(oldsymbol{u}_n) + oldsymbol{c}_n oldsymbol{M}_n) & oldsymbol{d}_n \ oldsymbol{0} & oldsymbol{0} \end{bmatrix} & oldsymbol{0} & oldsymbol{0} \end{bmatrix} & oldsymbol{0} & oldsymbol{0} \end{bmatrix} & oldsymbol{0} & oldsymbol{0} & oldsymbol{0} \end{bmatrix} & oldsymbol{0} & oldsymbol{0} & oldsymbol{0} \end{bmatrix} & oldsymbol{0} & oldsymbol{0} \end{bmatrix} & oldsymbol{0} & oldsymbol{0} & oldsymbol{0} & oldsymbol{0} \end{bmatrix} & oldsymbol{0} & oldsymbol{0} & oldsymbol{0} & oldsymbol{0} & oldsymbol{0} & oldsymbol{0} \end{bmatrix} & oldsymbol{0} & oldsym$$

with $A_s(\tilde{\mu}_m) := \sum_{q=1}^2 (\tilde{\mu}_m)_{q+1} A_s^q$. Here, $c_s \in \mathbb{R}^+$ is a parameter that encodes the elastic response of the surrounding tissues.

Eq.(2.4) can be conveniently rewritten as a monolithic N^{st} -dimensional nonlinear system — with $N^{st} := N^s N^t$ — as follows:

where the vectors $\boldsymbol{u}^{st} \in \mathbb{R}^{N_u^{st}}$, $\boldsymbol{p}^{st} \in \mathbb{R}^{N_p^{st}}$, $\boldsymbol{\lambda}^{st} \in \mathbb{R}^{N_\lambda^{st}}$, $\boldsymbol{d}^{st} \in \mathbb{R}^{N_u^{st}}$ collect, respectively, the full-order velocity, pressure, Lagrange multipliers and displacement discrete solutions, at the time instants $\{t_n\}_{n=1}^{N^t}$. The matrices \boldsymbol{A}_i^{st} ($i \in \{2,3,4,7\}$) and the vector \boldsymbol{F}_3^{st} are identical to the ones defined in [18] for the Stokes problem (see Eqs. (2.10), (2.11)). The matrix $\boldsymbol{A}_1^{st} \in \mathbb{R}^{N_u^{st} \times N_u^{st}}$ differs from the one reported in [18] due to the resistance boundary conditions. Indeed, we have

$$\boldsymbol{A}_{1}^{st} = \operatorname{diag}\left(\underbrace{\boldsymbol{M}, \cdots, \boldsymbol{M}}_{N^{t}}\right) + \beta \Delta t \operatorname{diag}\left(\underbrace{\boldsymbol{A} + \boldsymbol{R}, \cdots, \boldsymbol{A} + \boldsymbol{R}}_{N^{t}}\right) - \sum_{s=1}^{S} \alpha_{s} \operatorname{subdiag}^{(s)}\left(\underbrace{\boldsymbol{M}, \cdots, \boldsymbol{M}}_{N^{t}-s}\right),$$

where the operator diag: $\mathbb{R}^{r_1 \times c_1} \times \cdots \times \mathbb{R}^{r_K \times c_K} \to \mathbb{R}^{(r_1 + \cdots + r_K) \times (c_1 + \cdots + c_K)}$ builds a block diagonal matrix from a set of K input matrices; subdiag⁽ⁿ⁾ $(n \in \mathbb{N})$ is equivalent to diag, but with respect to the n-th subdiagonal. The term $e^{st}(u^{st}) \in \mathbb{R}^{N_u^{st}}$ represents the full-order nonlinear convective term evaluated at all the discrete time instants, multiplied by the positive constant $\beta \Delta t$. Finally, the matrices $A_s^{st}(\tilde{\mu}_m)$, M_s^{st} , and E_s^{st} , all of size $N_u^{st} \times N_u^{st}$ and

stemming from the coupled momentum model, are defined as follows:

$$\mathbf{A}_{s}^{st}(\tilde{\boldsymbol{\mu}}_{m}) = \sum_{q=1}^{2} (\tilde{\boldsymbol{\mu}}_{m})_{q+1} \, \mathbf{A}_{s}^{st,q} \quad \text{with} \quad \mathbf{A}_{s}^{st,q} = \beta \Delta t \, \operatorname{diag}\left(\underbrace{\mathbf{A}_{s}^{q}, \cdots, \mathbf{A}_{s}^{q}}_{N^{t}}\right);$$

$$\mathbf{M}_{s}^{st} = \operatorname{diag}\left(\underbrace{\mathbf{M}_{s}, \cdots, \mathbf{M}_{s}}_{N^{t}}\right) - \sum_{s=1}^{S} \alpha_{s} \, \operatorname{subdiag}^{(s)}\left(\underbrace{\mathbf{M}_{s}, \cdots, \mathbf{M}_{s}}_{N^{t}-s}\right);$$

$$\mathbf{E}_{s}^{st} = \beta \Delta t \, c_{s} \, \operatorname{diag}\left(\underbrace{\mathbf{M}_{s}, \cdots, \mathbf{M}_{s}}_{N^{t}}\right).$$
(2.6)

Adopting a more concise notation, we can rewrite Eq.(2.5) as follows:

$$\left(\mathbf{A}^{st} + \mathbf{A}^{\Gamma,st}(\tilde{\boldsymbol{\mu}}_{\boldsymbol{m}})\right) \boldsymbol{w}^{st} + \mathcal{E}_{u}\left(\boldsymbol{c}^{st}(\boldsymbol{u}^{st})\right) + \mathcal{E}_{u}\left(\left(\mathbf{A}_{\boldsymbol{s}}^{st}(\tilde{\boldsymbol{\mu}}_{\boldsymbol{m}}) + \boldsymbol{E}_{\boldsymbol{s}}^{st}\right) \boldsymbol{d}^{st}\right) = \boldsymbol{F}^{st}(\boldsymbol{\mu}_{\boldsymbol{f}}) + \boldsymbol{F}^{\Gamma,st}(\tilde{\boldsymbol{\mu}}_{\boldsymbol{m}}), \quad (2.7)$$

where $\boldsymbol{w}^{st} := [\boldsymbol{u}^{st}, \boldsymbol{p}^{st}, \boldsymbol{\lambda}^{st}] \in \mathbb{R}^{N^{st}}$ and $\boldsymbol{A}^{\Gamma,st}(\tilde{\boldsymbol{\mu}_m}) := \mathcal{E}_{u,u}(\boldsymbol{M}_s^{st}(\tilde{\boldsymbol{\mu}_m})) \in \mathbb{R}^{N^{st} \times N^{st}}$. The quantities $\boldsymbol{A}^{st} \in \mathbb{R}^{N^{st} \times N^{st}}$ and $\boldsymbol{F}^{st} \in \mathbb{R}^{N^{st}}$ are the left-hand side matrix and right-hand side vector components appearing in Eq.(2.5) that do not stem from the coupled momentum model. Here, the operators $\mathcal{E}_u : \mathbb{R}^{N_u^{st}} \to \mathbb{R}^{N^{st}}$ and $\mathcal{E}_{u,u} : \mathbb{R}^{N_u^{st} \times N_u^{st}} \to \mathbb{R}^{N^{st} \times N^{st}}$ denote the velocity zero–padding in one dimension and in two dimensions, respectively.

Remark 2.2 Eq.(2.5) is generic in what concerns the treatment of the membrane displacement. Such a formulation is convenient at this stage; in Section 3, we will propose different strategies to express \mathbf{d}^{st} in terms of the velocity field \mathbf{u}^{st} , depending on the chosen model order reduction approach.

Remark 2.3 The definitions of the matrices E_s^{st} and $A_s^{st}(\tilde{\mu}_m)$ in Eq.(2.6) entail that the membrane contributions are treated implicitly. In fact, in Eq.(2.5) we are not exploiting the kinematic coupling condition that links the displacement with the fluid velocity on Γ :

$$\underline{d}_h^{n+1} = \beta \Delta t \, \underline{u}_h^{n+1} + \sum_{s=1}^S \alpha_s \, \underline{d}_h^{n+1-s} \qquad \forall n \in \{0, \cdots, N^t - 1\} \,. \tag{2.8}$$

If the problem is solved iteratively over time, Eq.(2.8) allows to obtain, at every time instant, the displacement as a model by–product, combining the current velocity value and the displacement values available at S previous timesteps. We refer the reader to [27, 31, 28] for further details on this aspect.

3 ST-RB methods for the Coupled Momentum model

The traditional RB method operates only on the spatial dimensionality of the problem. Indeed, the projection is performed onto spatial subspaces, where the solution is sought at every time instant. Therefore, the temporal dimensionality of the problem does not change upon the reduction step, and the ODE stemming from the semi–discrete ROM is solved through iterative numerical integration. While in many applications this strategy is enough to guarantee a drastic downscaling on the computational costs, the efficacy of RB may not be entirely satisfactory in problems characterized by a large temporal complexity. For example, this is the case if either the simulation interval should be very large or the timestep size should be very small, to properly capture some relevant physical behaviours. In order to address such a temporal–complexity bottleneck, in this work we consider ST–RB methods [13, 15].

3.1 Space-time model order reduction

ST–RB methods are based on the assumption that good approximations of high–fidelity solutions over the entire spatio–temporal domain can be found within a linear subspace, spanned by a small number of spatio–temporal basis functions. To reduce the computational costs associated to the projection operations and the overall memory requirements, these methods express the space–time basis functions as multiplications of spatial and temporal modes. Let

$$\boldsymbol{\Phi}^{u} := \left[\boldsymbol{\varphi}_{1}^{u}\big|\cdots\big|\boldsymbol{\varphi}_{n_{u}^{s}}^{u}\right] \; \in \mathbb{R}^{N_{u}^{s}\times n_{u}^{s}} \; ; \qquad \boldsymbol{\Phi}^{p} := \left[\boldsymbol{\varphi}_{1}^{p}\big|\cdots\big|\boldsymbol{\varphi}_{n_{p}^{s}}^{p}\right] \; \in \mathbb{R}^{N_{p}^{s}\times n_{p}^{s}} \; ; \qquad \boldsymbol{\Phi}^{\lambda} := \left[\boldsymbol{\varphi}_{1}^{\lambda}\big|\cdots\big|\boldsymbol{\varphi}_{n_{\lambda}^{\lambda}}^{\lambda}\right] \; \in \mathbb{R}^{N_{\lambda}\times n_{\lambda}^{s}} \; ;$$

encode the discrete reduced basis functions in space and

$$\boldsymbol{\Psi}^{u} := \begin{bmatrix} \boldsymbol{\psi}_{1}^{u} \big| \cdots \big| \boldsymbol{\psi}_{n_{u}^{t}}^{u} \end{bmatrix} \; \in \mathbb{R}^{N^{t} \times n_{u}^{t}} \; ; \qquad \boldsymbol{\Psi}^{p} := \begin{bmatrix} \boldsymbol{\psi}_{1}^{p} \big| \cdots \big| \boldsymbol{\psi}_{n_{p}^{t}}^{p} \end{bmatrix} \; \in \mathbb{R}^{N^{t} \times n_{p}^{t}} \; ; \qquad \boldsymbol{\Psi}^{\lambda} := \begin{bmatrix} \boldsymbol{\psi}_{1}^{\lambda} \big| \cdots \big| \boldsymbol{\psi}_{n_{\lambda}^{t}}^{\lambda} \end{bmatrix} \; \in \mathbb{R}^{N^{t} \times n_{u}^{t}} \; ;$$

encode the discrete reduced basis functions in time, for velocity, pressure and Lagrange multipliers, respectively. All the reduced bases are computed following the ST-HOSVD approach proposed in [13]. In particular, we apply a randomized truncated POD algorithm [37] to the matrices storing high-fidelity solutions, corresponding to the parameter values $\{\mu_k\}_{k=1}^M$. The generic parameter vector μ_k is such that $\mu_k := [\mu_f^k, \mu_m^k] \in \mathcal{P} \subset \mathbb{R}^{N_\mu^f + N_\mu^m}$, with $\mu_f^k \in \mathcal{P}_f \subset \mathbb{R}^{N_\mu^f}$ and $\mu_m^k \in \mathcal{P}_m \subset \mathbb{R}^{N_\mu^m}$. We highlight that all the temporal bases are orthonormal with respect to the Euclidean norm in \mathbb{R}^{N^t} , whereas the spatial bases for velocity and pressure are orthonormal with respect to the $[H^1(\Omega)]^3$ -norm and to the $L^2(\Omega)$ -norm, respectively. We refer the reader to [18] for a detailed explanation of the reduced bases generation process.

We can now define the spatio-temporal discrete reduced basis functions as follows:

$$\begin{split} & \boldsymbol{\pi}_{\ell}^{u} \in \mathbb{R}^{N_{u}^{st}} & \text{ such that } & \boldsymbol{\pi}_{\ell}^{u} = \boldsymbol{\varphi}_{\ell_{s}}^{u} \otimes \boldsymbol{\psi}_{\ell_{t}}^{u} & \text{ with } \ell = (\ell_{s}-1)n_{u}^{t} + \ell_{t} =: \mathcal{F}_{u}(\ell_{s},\ell_{t}) \ ; \\ & \boldsymbol{\pi}_{k}^{p} \in \mathbb{R}^{N_{p}^{st}} & \text{ such that } & \boldsymbol{\pi}_{k}^{u} = \boldsymbol{\varphi}_{k_{s}}^{p} \otimes \boldsymbol{\psi}_{k_{t}}^{p} & \text{ with } k = (k_{s}-1)n_{p}^{t} + k_{t} =: \mathcal{F}_{p}(k_{s},k_{t}) \ ; \\ & \boldsymbol{\pi}_{i}^{\lambda} \in \mathbb{R}^{N_{\lambda}^{st}} & \text{ such that } & \boldsymbol{\pi}_{i}^{\lambda} = \boldsymbol{\varphi}_{i_{s}}^{\lambda} \otimes \boldsymbol{\psi}_{i_{t}}^{\lambda} & \text{ with } i = (i_{s}-1)n_{\lambda}^{t} + i_{t} =: \mathcal{F}_{\lambda}(i_{s},i_{t}) \ . \end{split}$$

Furthermore, we define the space-time-reduced dimensions $n_u^{st}:=n_u^s n_u^t, \ n_p^{st}:=n_p^s n_p^t, \ n_\lambda^{st}:=n_\lambda^s n_\lambda^t$ and $n^{st}:=n_u^{st}+n_p^{st}+n_\lambda^{st}$. We remark that the orthonormality of the reduced bases in space and in time induces the orthonormality of the spatio-temporal reduced bases, with respect to the natural norms in space-time. An approximate spatio-temporal basis for FOM solutions manifold can be then encoded in the matrix:

$$\boldsymbol{\Pi} := \operatorname{diag}\left(\left[\boldsymbol{\pi}_1^u|...|\boldsymbol{\pi}_{n_{s_t}^{s_t}}^u\right], \left[\boldsymbol{\pi}_1^p|...|\boldsymbol{\pi}_{n_{p_t}^{s_t}}^p\right], \left[\boldsymbol{\pi}_1^{\lambda}|...|\boldsymbol{\pi}_{n_{s_t}^{\lambda}}^{\lambda}\right]\right) = \operatorname{diag}\left(\boldsymbol{\Pi}^u, \boldsymbol{\Pi}^p, \boldsymbol{\Pi}^{\lambda}\right) \quad \in \mathbb{R}^{N^{st} \times n^{st}} \; .$$

The orthonormality of the spatio-temporal reduced bases qualifies Π^T as representative of an orthogonal projection operator from the FOM space of dimension N^{st} to the ST-ROM space of dimension $n^{st} \ll N^{st}$. Ultimately, we can define the space-time-reduced velocity $\hat{u} \in \mathbb{R}^{n_u^{st}}$, pressure $\hat{p} \in \mathbb{R}^{n_p^{st}}$ and Lagrange multipliers $\hat{\lambda} \in \mathbb{R}^{n_\lambda^{st}}$ such that:

$$m{u}^{st} pprox \sum_{\ell=1}^{n_u^{st}} \widehat{m{u}}_\ell m{\pi}_\ell^u \; ; \qquad m{p}^{st} pprox \sum_{k=1}^{n_p^{st}} \widehat{m{p}}_k m{\pi}_k^p \; ; \qquad m{\lambda}^{st} pprox \sum_{i=1}^{n_\lambda^{st}} \widehat{m{\lambda}}_i m{\pi}_i^\lambda \; .$$

For the sake of simplicity, from now on we will adopt the following notation for the indices of space-time-reduced quantities:

$$\ell = \mathcal{F}_{u}(\ell_{s}, \ell_{t}), \quad m = \mathcal{F}_{u}(m_{s}, m_{t}) \quad \text{with } \ell_{s}, m_{s} \in \{1, \cdots, n_{u}^{s}\}, \quad \ell_{t}, m_{t} \in \{1, \cdots, n_{u}^{t}\};$$

$$k = \mathcal{F}_{p}(k_{s}, k_{t}), \quad r = \mathcal{F}_{p}(r_{s}, r_{t}) \quad \text{with } k_{s}, r_{s} \in \{1, \cdots, n_{p}^{s}\}, \quad k_{t}, r_{t} \in \{1, \cdots, n_{p}^{t}\};$$

$$i = \mathcal{F}_{\lambda}(i_{s}, i_{t}), \quad j = \mathcal{F}_{\lambda}(j_{s}, j_{t}) \quad \text{with } i_{s}, j_{s} \in \{1, \cdots, N_{\lambda}\}, \quad i_{t}, j_{t} \in \{1, \cdots, n_{\lambda}^{t}\}.$$

Compared to the Navier–Stokes equations, the coupled momentum model features the presence of an additional unknown: the vessel wall displacement \underline{d} . However, the latter can be embodied in the Navier–Stokes equations, exploiting its kinematic coupling with the fluid velocity. As discussed in Section 2.2, if the problem is solved iteratively over time, this can be achieved exploiting Eq.(2.8). However, such a strategy does not produce any computational advantage if the temporal dynamics are projected onto a low–dimensional subspace. Indeed, in this setting the reduced solution encodes the displacement values at all the discrete time instants and the displacement does not be seamlessly configure as a model by–product. However, to strongly enforce the kinematic coupling condition under space–time model order reduction, we can approximate the spatio–temporal displacement field $d^{st} \in \mathbb{R}^{N_u^{st}}$ as

$$\boldsymbol{d}^{st} \approx \sum_{\ell=1}^{n_u^{st}} \widehat{\boldsymbol{u}}_{\ell} \boldsymbol{\pi}_{\ell}^d = \sum_{\ell=1}^{n_u^{st}} \widehat{\boldsymbol{u}}_{\ell} \left(\boldsymbol{\varphi}_{\ell_s}^u \otimes \mathcal{P}_0 \left(\mathcal{E}_S^t \left(\boldsymbol{\psi}_{\ell_t}^u \right) \right) \right) . \tag{3.1}$$

In Eq.(3.1), $\mathcal{E}_S^t: \mathbb{R}^{N^t} \to \mathbb{R}^{N^t+S}$ is a zero–padding operator, adding S zero entries at the beginning of its input. The operator $\mathcal{P}_0: \mathbb{R}^{N^t+S} \to \mathbb{R}^{N^t}$ denotes instead the numerical approximation of the primitive through the chosen multistep method, under the assumption that its input is equal to zero at the first S timesteps. In particular, the following recursive relation holds:

$$\left(\mathcal{P}_0(\boldsymbol{v})\right)_{n+1} = \beta \Delta t \, \boldsymbol{v}_{n+1} + \sum_{s=1}^{S} \alpha_s \left(\mathcal{P}_0(\boldsymbol{v})\right)_{n+1-s} \qquad \forall n \in \{0, \cdots, N^t - 1\}.$$

Eq.(3.1) allows to express the displacement as a function of the reduced velocity coefficients, while strongly enforcing the kinematic coupling condition. Therefore, the displacement no longer configures as a problem unknown and can be retrieved as a by–product during the post–processing phase. In fact, this is achieved through a projection onto a convenient spatio–temporal subspace. The latter is defined as the product space, generated by the velocity reduced subspace in space and by the subspace spanned by the primitives of the velocity modes in time. The vectors $\{\pi_{\ell}^d\}_{\ell=1}^{n_u^{st}}$ are stored as the columns of the matrix

$$\mathbf{\Pi}^d := \mathbf{\Phi}^u \otimes \mathcal{P}_0(\mathcal{E}_S^t(\mathbf{\Psi}^u)) \in \mathbb{R}^{N_u^{st} \times n_u^{st}}, \tag{3.2}$$

that encodes an approximate low–dimensional basis for the FOM displacement solutions manifold. In Eq.(3.2), the operators \mathcal{P}_0 and \mathcal{E}_S^t are defined as in Eq.(3.1), but they are applied columnwise. Thanks to Eq.(3.2), we can write $\mathbf{d}^{st} \approx \mathbf{\Pi}^d \widehat{\mathbf{u}}$.

3.2 ST-RB problem definition

From an algebraic standpoint, the application of the ST–RB method to Eq.(2.7) requires to find $\widehat{w} = [\widehat{u}, \widehat{p}, \widehat{\lambda}] \in \mathbb{R}^{n^{st}}$ such that

$$\widehat{r}(\widehat{\boldsymbol{w}}) := \widetilde{\boldsymbol{\Pi}}^T \left(\boldsymbol{F}^{st}(\boldsymbol{\mu_f}) - \left(\boldsymbol{A}^{st} + \boldsymbol{A}^{\Gamma,st}(\tilde{\boldsymbol{\mu}_m}) \right) \boldsymbol{\Pi} \widehat{\boldsymbol{w}} - \mathcal{E}_u \left(\boldsymbol{c}^{st} \left(\boldsymbol{\Pi}^u \widehat{\boldsymbol{u}} \right) + \left(\boldsymbol{A}_s^{st}(\tilde{\boldsymbol{\mu}_m}) + \boldsymbol{E}_s^{st} \right) \boldsymbol{\Pi}^d \widehat{\boldsymbol{u}} \right) \right) = \boldsymbol{0} \ . \tag{3.3}$$

Here $\widetilde{\Pi} \in \mathbb{R}^{N^{st} \times n^{st}}$ is a possibly parameter-dependent matrix, while \mathcal{E}_u is the zero-padding operator used in Eq.(2.7). Eq.(3.3) prescribes the orthogonality between the approximate FOM residual — evaluated at the high-fidelity reconstruction of the space-time-reduced solution $\widehat{w}^{st} := \Pi \widehat{w} \in \mathbb{R}^{N^{st}}$ — and a low-dimensional subspace, spanned by the columns of $\widetilde{\Pi}$. Different ST-RB methods stem from different choices of $\widetilde{\Pi}$. In [18], two special cases have been investigated: the first stems from the trivial choice $\widetilde{\Pi} = \Pi$ (Galerkin projection, ST-GRB method), whereas the second arises from the least-squares minimization of the FOM residual in a suitable norm (least-squares Petrov-Galerkin projection, ST-PGRB method). In this work, we focus only on the ST-GRB method. Nonetheless, we highlight that a similar analysis can be carried out whenever the matrix $\widetilde{\Pi}$ is parameter-independent. It is worth remarking that, in the case of Galerkin projections, suitable augmentations of the spatial and temporal velocity reduced basis are required to guarantee the *inf-sup* stability, and hence the well-posedness, of the problem. We refer the reader to [38] for the supremizers enrichment procedure in space and to [18] for the stabilizers enrichment procedure in time.

Eq.(3.3) describes a n^{st} -dimensional nonlinear system, whose nonlinearity is due to the presence of the convective term $c(\Pi^u \widehat{u})$. If the Navier–Stokes equations are solved iteratively over time, it is a popular strategy to linearize the convective term, by extrapolation in time of the velocity solutions available at previous time instants. However, as already discussed concerning the treatment of the coupled momentum model contributions, the use of a monolithic space–time formulation to enable the compression of the temporal dynamics nullifies the computational gains of this approach. Therefore, the nonlinear nature of the problem cannot be easily circumvented and Eq.(3.3) should be solved adopting ad hoc numerical techniques. In this work, we rely on the Newton–Raphson method. Let $\widehat{w}^{(0)} \in \mathbb{R}^{n^{st}}$ be a given initial guess; the superscript denotes the iteration index. Then, the solution to Eq.(3.3) is iteratively found as follows:

$$\widehat{\boldsymbol{w}}^{(l+1)} = \widehat{\boldsymbol{w}}^{(l)} - \left(\widehat{\boldsymbol{J}}_{\widehat{\boldsymbol{r}}}(\widehat{\boldsymbol{w}}^{(l)})\right)^{-1} \widehat{\boldsymbol{r}}(\widehat{\boldsymbol{w}}^{(l)}) \quad \text{with} \quad \left(\widehat{\boldsymbol{J}}_{\widehat{\boldsymbol{r}}}(\widehat{\boldsymbol{w}}^{(l)})\right)_{ij} := \left.\frac{\partial \widehat{\boldsymbol{r}}_i}{\partial \widehat{\boldsymbol{w}}_j}\right|_{\widehat{\boldsymbol{w}} = \widehat{\boldsymbol{w}}^{(l)}}, \quad (3.4)$$

where the matrix $\widehat{J}_{\widehat{r}} \in \mathbb{R}^{n^{st} \times n^{st}}$ denotes the Jacobian of the residual $\widehat{r} \in \mathbb{R}^{n^{st}}$ with respect to the space-time-reduced solution \widehat{w} . From Eq.(3.3), setting $\widetilde{\Pi} = \Pi$ (ST-GRB method), we have that

$$\widehat{J}_{\widehat{r}}(\widehat{w}) = -\Pi^{T} \left(A^{st} + A^{\Gamma,st}(\widetilde{\mu}_{m}) \right) \Pi - \Pi^{T} \mathcal{E}_{u,u} \left(J_{c}^{st}(\Pi^{u}\widehat{u}) \right) \Pi - \Pi^{T} \mathcal{E}_{u,u} \left(A_{s}^{st}(\widetilde{\mu}_{m}) + E_{s}^{st} \right) \Pi^{d}, \quad (3.5)$$

where $J_c^{st}(\Pi^u \widehat{u}) \in \mathbb{R}^{N_u^{st} \times N_u^{st}}$ is a block-diagonal matrix containing the full-order convective Jacobian matrices, evaluated at the reconstructed reduced velocity solution for all the discrete time instants and multiplied by $\beta \Delta t$. Also, $\mathcal{E}_{u,u}$ is the zero-padding operator used in Eq.(2.7). The iterations in Eq.(3.4) are executed until the following condition is satisfied:

$$\left\|\widehat{\boldsymbol{r}}(\widehat{\boldsymbol{w}}^{(l)})\right\|_{2} / \left\|\widehat{\boldsymbol{r}}(\widehat{\boldsymbol{w}}^{(0)})\right\|_{2} \le \tau_{NR}, \qquad (3.6)$$

where $\tau_{NR} \in \mathbb{R}^+$ is a user–provided tolerance. If the stopping criterion in Eq.(3.6) is not reached after $K_{NR} \in \mathbb{N}$ iterations (at most), then we say that the Newton–Raphson method does not converge.

3.3 Assembling the reduced system

In this section, we discuss how the space-time-reduced residual $\hat{r}(\hat{w})$ (see Eq.(3.3)) and its Jacobian $\hat{J}_{\hat{r}}(\hat{w})$ (see Eq.(3.5)) can be efficiently assembled. It is worth remarking that the affine parametrization of the problem enables the offline computation of several space-time-reduced quantities. This allows to drastically lower the online computational costs and to maximize speedups at no loss in accuracy. In the general case, approximate affine decompositions can be retrieved via the Discrete Empirical Interpolation Method (DEIM) [39] or its matricial version MDEIM [40].

To simplify the notation, we rewrite the space-time-reduced residual and its Jacobian as follows:

$$\widehat{\boldsymbol{r}}(\widehat{\boldsymbol{w}}) = \widehat{\boldsymbol{F}}(\boldsymbol{\mu_f}) - \left(\widehat{\boldsymbol{A}} + \widehat{\boldsymbol{A}}^{\Gamma}(\widetilde{\boldsymbol{\mu}_m})\right)\widehat{\boldsymbol{w}} - \widehat{\mathcal{E}}_u(\widehat{\boldsymbol{c}}(\widehat{\boldsymbol{a}})) - \widehat{\mathcal{E}}_u((\widehat{\boldsymbol{A}}_s(\widetilde{\boldsymbol{\mu}_m}) + \widehat{\boldsymbol{E}}_s)\widehat{\boldsymbol{u}}); \tag{3.7a}$$

$$\widehat{J}_{\widehat{r}}(\widehat{w}) = -\left(\widehat{A} + \widehat{A}^{\Gamma}(\widetilde{\mu}_{m})\right) - \widehat{\mathcal{E}}_{u,u}(\widehat{J}_{c}(\widehat{u})) - \widehat{\mathcal{E}}_{u,u}(\widehat{A}_{s}(\widetilde{\mu}_{m}) + \widehat{E}_{s});$$
(3.7b)

where $\widehat{\mathcal{E}}_u: \mathbb{R}^{n_u^{st}} \to \mathbb{R}^{n^{st}}$ and $\widehat{\mathcal{E}}_{u,u}: \mathbb{R}^{n_u^{st} \times n_u^{st}} \to \mathbb{R}^{n^{st} \times n^{st}}$ are the vectorial and the matricial space–time–reduced velocity zero–padding operators, respectively. The quantities appearing in Eq.(3.7) will be suitably defined throughout this section. Before detailing how the reduced system is assembled, let us introduce the following space–reduced quantities:

- the matrices $\overline{M} \in \mathbb{R}^{n_u^s \times n_u^s}$, $\overline{A} \in \mathbb{R}^{n_u^s \times n_u^s}$, $\overline{B} \in \mathbb{R}^{n_u^s \times n_p^s}$, $\overline{L} \in \mathbb{R}^{n_u^s \times N_\lambda}$, $\overline{B}^T \in \mathbb{R}^{n_p^s \times n_u^s}$, $\overline{L}^T \in \mathbb{R}^{N_\lambda \times n_u^s}$, $\overline{R}^T \in \mathbb{R}^{n_u^s \times n_u^s}$, that are the space-reduced counterparts of the FOM matrices M, A, B, L, B^T , L^T , R, respectively. For example, $\overline{M} := (\Phi^u)^T M \Phi^u$.
- the matrices $\overline{M}_s \in \mathbb{R}^{n_u^s \times n_u^s}$ and $\{\overline{A}_s^q\}_{q=1}^2 \in \mathbb{R}^{n_u^s \times n_u^s}$, that are the space-reduced counterparts of the FOM structure matrices M_s and $\{A_s^q\}_{q=1}^2$, respectively. In particular, $\overline{M}_s := (\Phi^u)^T M_s \Phi^u$; $\overline{A}_s^q := (\Phi^u)^T A_s^q \Phi^u$ for q=1,2.

3.3.1 Space-time-reduced linear terms

The assembling of the parameter–independent space–time–reduced left–hand side matrix $\widehat{A} := \Pi^T A \Pi \in \mathbb{R}^{n^{st} \times n^{st}}$ is analogous to the Stokes case [18], besides including the resistance boundary conditions contributions. Hence, \widehat{A} has the following block structure

$$\widehat{m{A}} = egin{bmatrix} \widehat{m{A}}_1 & \widehat{m{A}}_2 & \widehat{m{A}}_3 \ \widehat{m{A}}_4 & m{0} & m{0} \ \widehat{m{A}}_7 & m{0} & m{0} \end{bmatrix} \; ,$$

and the entries of the matrices in the non-zero blocks are

$$\begin{pmatrix} \widehat{\boldsymbol{A}}_{1} \end{pmatrix}_{\ell m} = \left(\overline{\boldsymbol{M}} + \beta \Delta t \left(\overline{\boldsymbol{A}} + \overline{\boldsymbol{R}} \right) \right)_{\ell_{s} m_{s}} \delta_{\ell_{t}, m_{t}} - \sum_{s=1}^{S} \alpha_{s} \, \overline{\boldsymbol{M}}_{\ell_{s} m_{s}} \left((\boldsymbol{\psi}_{\ell_{t}}^{u})_{s+1:}^{T} (\boldsymbol{\psi}_{m_{t}}^{u})_{:-s} \right),
\begin{pmatrix} \widehat{\boldsymbol{A}}_{2} \end{pmatrix}_{\ell r} = \beta \Delta t \, \overline{\boldsymbol{B}}_{\ell_{s} r_{s}}^{T} \left((\boldsymbol{\psi}_{\ell_{t}}^{u})^{T} (\boldsymbol{\psi}_{r_{t}}^{p}) \right),
\begin{pmatrix} \widehat{\boldsymbol{A}}_{3} \end{pmatrix}_{\ell j} = \beta \Delta t \, \overline{\boldsymbol{L}}_{\ell_{s} j_{s}}^{T} \left((\boldsymbol{\psi}_{\ell_{t}}^{u})^{T} (\boldsymbol{\psi}_{j_{t}}^{\lambda}) \right),
\begin{pmatrix} \widehat{\boldsymbol{A}}_{7} \end{pmatrix}_{im} = \overline{\boldsymbol{L}}_{i_{s} m_{s}} \left((\boldsymbol{\psi}_{i_{t}}^{\lambda})^{T} (\boldsymbol{\psi}_{m_{t}}^{u}) \right).$$

Here the notations $v_{i:}$, $v_{:-i}$ denote the sub-vector of a given vector v containing all the entries from the i-th to the last one and from the first one to the i-th from last, respectively. From Eq.(2.5), we notice that the coupled momentum model adds a parametrized boundary mass term in the velocity-velocity block. Therefore, we define the matrix $\widehat{A}^{\Gamma}(\widetilde{\mu}_m) := (\widetilde{\mu}_m)_1 \ \widehat{\mathcal{E}}_{u,u}(\widehat{M}_s)$; exploiting the tridiagonal block structure of M_s^{st} (see Eq.(2.6)), we have

$$\left(\widehat{\boldsymbol{M}}_{\boldsymbol{s}}\right)_{\ell m} = (\overline{\boldsymbol{M}}_{\boldsymbol{s}})_{\ell_s m_s} \delta_{\ell_t, m_t} - \sum_{s=1}^{S} \alpha_s (\overline{\boldsymbol{M}}_{\boldsymbol{s}})_{\ell_s m_s} \left((\boldsymbol{\psi}_{\ell_t}^u)_{s+1:}^T (\boldsymbol{\psi}_{m_t}^u)_{:-s} \right).$$

The coupled momentum model introduces a boundary stiffness matrix featuring a single non-zero block in the velocity-velocity compartment. Since the space-time-reduced basis matrix Π is block-diagonal, the same block structure is maintained upon the projection. Leveraging the affine parametrization and the block-diagonal structure

of A_s^{st} (see Eq.(2.6)), and exploiting the space–time approximation of the displacement field reported in Eq.(3.1), we have that

$$\widehat{\boldsymbol{A}}_{\boldsymbol{s}}(\widetilde{\boldsymbol{\mu}}_{\boldsymbol{m}}) = \beta \Delta t \, \sum_{q=1}^{2} (\widetilde{\boldsymbol{\mu}}_{\boldsymbol{m}})_{q+1} \, \widehat{\boldsymbol{A}}_{\boldsymbol{s}}^{q} \quad \text{with} \quad \left(\widehat{\boldsymbol{A}}_{\boldsymbol{s}}^{q}\right)_{\ell_{m}} = \left(\overline{\boldsymbol{A}}_{\boldsymbol{s}}^{q}\right)_{\ell_{s}m_{s}} \left(\left(\boldsymbol{\psi}_{\ell_{t}}^{u}\right)^{T} \left(\mathcal{P}_{0}\left(\mathcal{E}_{S}^{t}\left(\boldsymbol{\psi}_{m_{t}}^{u}\right)\right)\right)\right).$$

Similarly, the surrounding tissues contribution is encoded in the matrix \hat{E}_s , whose entries are

$$\left(\widehat{\boldsymbol{E}}_{\boldsymbol{s}}\right)_{\ell m} = \beta \Delta t \ c_{s} \left(\overline{\boldsymbol{M}}_{\boldsymbol{s}}\right)_{\ell_{s} m_{s}} \left(\left(\boldsymbol{\psi}_{\ell_{t}}^{u}\right)^{T} \left(\mathcal{P}_{0}\left(\mathcal{E}_{S}^{t}\left(\boldsymbol{\psi}_{m_{t}}^{u}\right)\right)\right)\right).$$

The space-time-reduced residual $\widehat{r}(\widehat{w})$ features a single non-zero block $\widehat{F}_3(\mu_f) := \Pi_\lambda^T F_3^{st}(\mu_f)$ in right-hand side vector. The non-affine parameter-dependent nature of F_3^{st} implies that \widehat{F}_3 cannot be pre-assembled during the offline phase. However, we can take advantage of the space-time factorization of the Dirichlet datum in Eq.(2.3) and, in particular, of the fact that the parametric dependency characterizes only the (discretized) flow rates $g_k^t(\mu_f) \in \mathbb{R}^{N^t}$, with $k=1,\cdots,N_D$. Indeed, the k-th block of the space-time reduced right-hand side $\widehat{F}_{3,k}(\mu_f)$ is such that

$$\widehat{\pmb{F}}_{3,k}(\pmb{\mu_f}) \in \mathbb{R}^{n_{\lambda_k}^{st}} \quad \text{with} \ \left(\widehat{\pmb{F}}_{3,k}\right)_{i^k} = \beta \Delta t \ \left(\left(\varphi_{i_s^k}^{\lambda_k}\right)^T \pmb{g}_k^s\right) \ \left(\left(\pmb{\psi}_{i_t^k}^{\lambda_k}\right)^T \pmb{g}_k^t(\pmb{\mu_f})\right) \ ,$$

where $i^k = \mathcal{F}_{\lambda_k}(i^k_s, i^k_t) := (i^k_s - 1)n^t_{\lambda_k} + i^k_t$. Ultimately, leveraging the product structure of the Lagrange multipliers subspace, we have

$$\widehat{\boldsymbol{F}}_{3}(\boldsymbol{\mu_{f}}) = \left[\left(\widehat{\boldsymbol{F}}_{3,1}(\boldsymbol{\mu_{f}}) \right)^{T}, \cdots, \left(\widehat{\boldsymbol{F}}_{3,N_{D}}(\boldsymbol{\mu_{f}}) \right)^{T} \right]^{T} \in \mathbb{R}^{n_{\lambda}^{st}}.$$

We remark that this assembling step is extremely cheap, since it involves N_D matrix-vector products of dimension N^t .

3.3.2 Space-time-reduced nonlinear convective term

The presence of the nonlinear convective term is what differentiates the Navier–Stokes equations from the Stokes equations. As discussed in Section 3.2, the linearization of the convective term by means of temporal extrapolation does not load to significant computational gains within the ST–RB framework; so, a fully–implicit approach is compulsory. The most straightforward strategy is to assemble the full–order convective term and project it onto the velocity reduced subspace. However, this inherently comes with several drawbacks. First of all, the associated computational costs are high, since they inherently depend on the high–fidelity dimensions in space–time. Indeed, at every Newton iteration, one should expand the space–time–reduced solution to the FOM space, compute the FOM convective term at all the discrete time instants and project it back again to the space–time–reduced subspace. Secondly, this procedure is intrusive at both the offline and the online stage, where by "intrusivity" we refer to the use of the FOM software during the ROM pipeline. While offline intrusivity characterizes the RB method, online intrusivity can represent a big limitation. Indeed, efficient communication routines between the FOM and the ROM softwares should be implemented, which not be trivial if closed–source programs are employed for the high–fidelity simulations.

To overcome the pitfalls of the baseline assembling approach, in this work we exploit the bilinearity of the convective term. For $\underline{u}_h, \underline{v}_h, \underline{w}_h \in \mathcal{V}_h$, the following affine decomposition holds [36]:

$$\rho_f \int_{\Omega} \left((\underline{u}_h \cdot \nabla) \, \underline{w}_h \right) \cdot \underline{v}_h =: a_{con} \left(\underline{u}_h, \underline{w}_h; \underline{v}_h \right) = \rho_f \sum_{i=1}^{N_u^s} \sum_{j=1}^{N_u^s} \boldsymbol{u}_i \, \boldsymbol{w}_j \, a_{con} \left(\underline{\varphi}_i^u, \underline{\varphi}_j^u; \underline{v}_h \right) , \qquad (3.8)$$

where $u, w \in \mathbb{R}^{N_u^s}$ are the FOM discrete representations of \underline{u}_h , \underline{w}_h . Even though Eq.(3.8) is written considering high-fidelity discretizations of the velocity, its extension to the space-reduced framework is trivial. Indeed, adopting an algebraic perspective, we can write the space-reduced convective term $\bar{c} \in \mathbb{R}^{n_u^s}$ as follows:

$$\bar{\boldsymbol{c}}(\bar{\boldsymbol{u}}) = \beta \Delta t \sum_{\ell_s'=1}^{n_u^s} \sum_{\ell_s''=1}^{n_u^s} \bar{\boldsymbol{u}}_{\ell_s'} \bar{\boldsymbol{k}}_{\ell_s' \ell_s''} \quad \text{with} \quad (\bar{\boldsymbol{k}}_{\ell_s' \ell_s''})_{m_s} = a_{con} \left(\underline{\phi}_{\ell_s'}^u, \underline{\phi}_{\ell_s''}^u; \underline{\phi}_{m_s}^u\right) , \tag{3.9}$$

where $\underline{\phi}^u_{\ell_s} \in \mathcal{V}_h$ is such that $\underline{\phi}^u_{\ell_s}(\underline{x}) := \sum_{i=1}^{N_u^s} (\Phi^u)_{i\ell_s} \, \underline{\varphi}^u_i(\underline{x})$ is the ℓ_s -th velocity reduced basis function in space and $\bar{\boldsymbol{u}} \in \mathbb{R}^{N_u^s}$ is the discrete representation of the space-reduced velocity field at an arbitrary time instant. We remark

that the vectors $\{\bar{k}_\ell\}_{\ell=1}^{(n_u^s)^2}$ are independent from the solution and thus can be pre-assembled during the offline phase. Hence, Eq.(3.9) shows that the space-reduced convective term exhibits an exact affine decomposition, whose weights stem from the outer product of the space-reduced solution \bar{u} with itself. A key implication of Eq.(3.9) is that the number of affine components depends quadratically on the number of velocity reduced bases, possibly limiting the computational advantages of the method. In this regard, to prevent efficiency losses, we can leverage the fact that the spatial velocity bases are sorted in decreasing order of "importance", since they have been computed through POD. Therefore, we can approximate the reduced nonlinear convective term with the following truncated expansion:

$$\bar{\boldsymbol{c}}(\bar{\boldsymbol{u}}) \approx \beta \Delta t \sum_{\ell'_{\cdot}=1}^{n_{c}} \sum_{\ell''_{\cdot}=1}^{n_{c}} \bar{\boldsymbol{u}}_{\ell'_{s}} \, \bar{\boldsymbol{k}}_{\ell'_{s}} \ell''_{s} , \quad \text{where } 0 \leq n_{c} \leq n_{u}^{s} . \tag{3.10}$$

The effect of the choice of n_c on the efficiency and accuracy of the method will be empirically investigated in Section 4.2.

To embed the nonlinear convective term in the ST-RB problem formulation of Eq.(3.3), we need to project Eq.(3.10) onto the space-time-reduced velocity subspace. To this aim, we observe that the space-reduced solution \bar{u}_n at time t_n can be written as a function of the space-time-reduced solution \hat{u} as follows:

$$\bar{\boldsymbol{u}}_n \in \mathbb{R}^{n_u^s}: \ (\bar{\boldsymbol{u}}_n)_{\ell_s} = \sum_{\ell_t=1}^{n_u^t} \widehat{\boldsymbol{u}}_\ell \ (\boldsymbol{\psi}_{\ell_t}^u)_n \quad \text{with } \ell = \mathcal{F}_u(\ell_s, \ell_t) \ . \tag{3.11}$$

Therefore, the space-time-reduced convective term $\widehat{c}(\widehat{u}) \in \mathbb{R}^{n_u^{st}}$ can be approximated as follows:

$$(\widehat{\boldsymbol{c}}(\widehat{\boldsymbol{u}}))_{m} \approx \beta \Delta t \sum_{n=1}^{N^{t}} \left(\sum_{\ell'_{s}=1}^{n_{c}} \sum_{\ell''_{s}=1}^{n_{c}} \left(\sum_{\ell'_{t}=1}^{n_{u}^{t}} \widehat{\boldsymbol{u}}_{\ell'}(\boldsymbol{\psi}_{\ell'_{t}}^{u})_{n} \right) \left(\sum_{\ell''_{t}=1}^{n_{u}^{t}} \widehat{\boldsymbol{u}}_{\ell''}(\boldsymbol{\psi}_{\ell''_{t}}^{u})_{n} \right) \bar{\boldsymbol{k}}_{\ell'_{s}\ell''_{s}} \right)_{m_{s}} (\boldsymbol{\psi}_{m_{t}}^{u})_{n}$$

$$= \beta \Delta t \sum_{\ell'_{s}=1}^{n_{c}} \sum_{\ell''_{s}=1}^{n_{c}} \left(\bar{\boldsymbol{k}}_{\ell'_{s}\ell''_{s}} \right)_{m_{s}} \sum_{\ell'_{s}=1}^{n_{u}^{t}} \sum_{\ell'_{s}=1}^{n_{u}^{t}} \widehat{\boldsymbol{u}}_{\ell'} \widehat{\boldsymbol{u}}_{\ell''} \boldsymbol{\psi}_{\ell'_{t},\ell''_{t},m_{t}}^{u,3},$$

$$(3.12)$$

where $\psi^{u,3}_{\ell'_t,\ell''_t,m_t} := \sum_n (\psi^u_{\ell'_t})_n (\psi^u_{\ell''_t})_n (\psi^u_{m_t})_n$. Since the quantities $\bar{k}_{\ell'_s\ell''_s}$ and $\psi^{u,3}_{\ell'_t,\ell''_t,m_t}$ can be pre–assembled offline, exploiting tensorial calculus the computation of $\hat{c}(\hat{u})$ reduces to a linear combination and becomes relatively cheap.

Solving the ST-RB problem with the Newton-Raphson method requires to assemble the space-time-reduced convective Jacobian matrix $\widehat{J}_c \in \mathbb{R}^{n_u^{st} \times n_u^{st}}$. To this aim, we exploit that the high-fidelity convective Jacobian operator $J_{con}: \mathcal{V}_h \to \mathbb{R}$ is linear; indeed for $\underline{u}_h, \underline{v}_h', \underline{v}_h'' in \mathcal{V}_h$, we have

$$J_{con}(\underline{u}_h; \underline{v}_h', \underline{v}_h'') = \int_{\Omega} \rho_f\left((\underline{v}_h'' \cdot \nabla) \underline{u}_h\right) \cdot \underline{v}_h' + \int_{\Omega} \rho_f\left((\underline{u}_h \cdot \nabla) \underline{v}_h''\right) \cdot \underline{v}_h'.$$

Hence, the following affine decomposition trivially holds for the space-reduced convective Jacobian $\bar{J}_c(\bar{u}) \in \mathbb{R}^{n_u^s \times n_u^s}$:

$$\overline{\boldsymbol{J}}_{\boldsymbol{c}}(\overline{\boldsymbol{u}}) = \sum_{\ell_s=1}^{n_u^s} \overline{\boldsymbol{u}}_{\ell_s} \overline{\boldsymbol{K}}_{\ell_s} \approx \sum_{\ell_s=1}^{n_{c,J}} \overline{\boldsymbol{u}}_{\ell_s} \overline{\boldsymbol{K}}_{\ell_s} \quad \text{with} \quad \left(\overline{\boldsymbol{K}}_{\ell_s}\right)_{m_s'm_s''} = J_{con}\left(\underline{\boldsymbol{\phi}}_{\ell_s}^u; \underline{\boldsymbol{\phi}}_{m_s'}^u, \underline{\boldsymbol{\phi}}_{m_s''}^u\right) \;,$$

where $0 \le n_{c,J} \le n_u^s$. Exploiting Eq.(3.11), we can then approximate the space–time–reduced convective Jacobian matrix $\widehat{J}_c(\widehat{u}) \in \mathbb{R}^{n_u^{st} \times n_u^{st}}$ as follows:

$$\left(\widehat{\boldsymbol{J}}_{\boldsymbol{c}}(\widehat{\boldsymbol{u}})\right)_{m'm''} \approx \beta \Delta t \sum_{n=1}^{N^{t}} \left(\sum_{\ell_{s}=1}^{n_{c,J}} \left(\sum_{\ell_{t}=1}^{n_{u}^{t}} \widehat{\boldsymbol{u}}_{\ell}(\boldsymbol{\psi}_{\ell_{t}}^{u})_{n}\right) \overline{\boldsymbol{K}}_{\ell_{s}}\right)_{m'_{s}m''_{s}} (\boldsymbol{\psi}_{m'_{t}}^{u})_{n}(\boldsymbol{\psi}_{m'_{t}}^{u})_{n}$$

$$= \beta \Delta t \sum_{\ell_{s}=1}^{n_{c,J}} \left(\overline{\boldsymbol{K}}_{\ell_{s}}\right)_{m'_{s}m''_{s}} \sum_{\ell_{t}=1}^{n_{u}^{t}} \widehat{\boldsymbol{u}}_{\ell} \, \boldsymbol{\psi}_{\ell_{t},m'_{t},m''_{t}}^{u,3}, \tag{3.13}$$

where the coefficients $\psi^{u,3}_{\ell_t,m'_t,m''_t}$ are defined as in Eq.(3.12). Once again, the possibility to pre–compute the quantities \bar{K}_{ℓ_s} and $\psi^{u,3}_{\ell_t,m'_t,m''_t}$ makes the assembling of $\hat{J}_c(\hat{u})$ relatively inexpensive.

Remark 3.1 The space-reduced convective term (and its Jacobian) can also be efficiently assembled using the (M)DEIM algorithm, which may actually yield more accurate affine decompositions for the same number of modes. However, (M)DEIM requires the evaluation of high-fidelity quantities in a select number of mesh nodes, hence introducing intrusivity at the online stage. Even though a non-intrusive pipeline could be recovered through interpolation techniques (see e.g. [41]), for the sake of simplicity we rely on the approximate affine decompositions reported in Eqs.(3.12), (3.13).

3.4 Online phase

The goal of the online phase is to efficiently compute the solution to Eq.(3.3) for a parameter instance

$$\boldsymbol{\mu}^* = [\boldsymbol{\mu_f^*}, \boldsymbol{\mu_m^*}] \in \mathcal{P} \subset \mathbb{R}^{N_\mu^f + N_\mu^m} \;, \quad \text{where} \;\; \boldsymbol{\mu_f^*} \in \mathcal{P}_f \subset \mathbb{R}^{N_\mu^f}, \; \boldsymbol{\mu_m^*} \in \mathcal{P}_m \subset \mathbb{R}^{N_\mu^m} \;,$$

that was not considered offline. As detailed in [18], it comprises three steps: the assembling of the reduced system, the computation of the reduced solution and its full-order reconstruction. The first step has fundamentally already been detailed in Section 3.3.

Dealing with a nonlinear problem, the computation of the space–time–reduced solution involves the sequential resolution of some "small" dense linear systems, whose number depends on the convergence of the Newton iterations. This entails that another means of achieving efficiency is by reducing the number of iterations needed to satisfy the stopping criterion in Eq.(3.6). To this aim, the choice of the initial guess $\widehat{\boldsymbol{w}}^{(0)} \in \mathbb{R}^{n^{st}}$ is crucial. In fact, the convergence properties of the Newton–Raphson method indicate that the closer $\widehat{\boldsymbol{w}}^{(0)}$ is to the reduced solution $\widehat{\boldsymbol{w}}(\boldsymbol{\mu}^*)$, the more likely and the faster the iterations converge. If no dimensionality reduction in time takes place, the initial guess can be selected either as the solution at the previous timestep or by extrapolation [42]. However, these are not viable strategies with ST–RB methods, for which the choice of $\widehat{\boldsymbol{w}}^{(0)}$ becomes less straightforward. Following [13], we decided to employ non–intrusive interpolation–based ROM approaches. So, let $\{\mu_k\}_{k=1}^M$ be the offline parameter values and $\{\widehat{\boldsymbol{w}}_k\}_{k=1}^M \in \mathbb{R}^{n^{st}}$ be the space–time projections of the corresponding FOM solutions, which can be pre–computed. Then, for a given $\boldsymbol{\mu}^* \in \mathcal{P}$, the initial guess is calculated via interpolation in the parameter space. In this work, we compare two approaches:

• Nearest Neighbours Interpolation (NNI):

$$\widehat{w}^{(0)}(\mu^*) = \sum_{k=1}^K \frac{||\mu^* - \mu_{\mathcal{S}(k)}||_2}{D} \widehat{w}_{\mathcal{S}(k)} \quad \text{with } D := \sum_{k=1}^K ||\mu^* - \mu_{\mathcal{S}(k)}||_2 ,$$

where S(k) denotes the index of the k-th closest parameter to μ^* within $\{\mu_k\}_{k=1}^M$ in Euclidean norm. The quantity $k \in \mathbb{N}$ is the number of considered nearest neighbours in the parameters' space.

• Proper Orthogonal Decomposition Interpolation (PODI) [43, 44]:

$$\left(\widehat{\boldsymbol{w}}^{(0)}(\boldsymbol{\mu}^*)\right)_{\ell} = \sum_{k=1}^{M} \boldsymbol{\vartheta}_{k}^{\ell} \zeta\left(||\boldsymbol{\mu}^* - \boldsymbol{\mu}_{k}||_{2}\right)
\text{with } \boldsymbol{\vartheta}^{\ell} \in \mathbb{R}^{M} : \boldsymbol{Z}\boldsymbol{\vartheta}^{\ell} = \boldsymbol{a}^{\ell}, \quad \left(\boldsymbol{Z}\right)_{k_{1}k_{2}} = \zeta\left(||\boldsymbol{\mu}_{k_{1}} - \boldsymbol{\mu}_{k_{2}}||_{2}\right), \, \left(\boldsymbol{a}^{\ell}\right)_{k} = \left(\widehat{\boldsymbol{w}}_{k}\right)_{\ell}.$$
(3.14)

Here $\zeta:\mathbb{R}^+\to\mathbb{R}$ is a kernel function; in this work we relied on thin–plate spline interpolation, hence choosing $\zeta(x)=x^2\ln(x)$. We underline that this approach entails solving, during the offline phase, n^{st} independent linear systems of dimension M. Since the left–hand side matrix Z is the same for all the systems, convenient factorizations can be exploited to speedup the computations.

Section 4.2 features an empirical comparison of the performances of NNI and PODI; the *naive* choices of selecting $\hat{w}^{(0)}$ either as the zero vector or as the average of the offline reduced solutions are also considered.

Remark 3.2 To further reduce the online computational costs, one can neglect the reduced Jacobian of the convective term $\widehat{J}_{\mathbf{c}}(\widehat{w})$ in Eq.(3.5), thus resorting to a quasi–Newton method. In the laminar flow regime, where viscous forces dominate over inertial effects, this should not significantly impact on the accuracy of the method, since the change in the reduced Jacobian $\widehat{J}_{\widehat{r}}$ is expected to be small. Nonetheless, this technique is particularly convenient because it keeps the Jacobian constant across the Newton iterations, hence enabling the use of LU factorization. The largest computational gains can be realized when the parametrization is confined to the right-hand side vector; an example is represented by test case reported in Section 4.2. Indeed, in such cases the LU factorization of the reduced Jacobian can be pre-computed, and only triangular systems are left to be solved online.

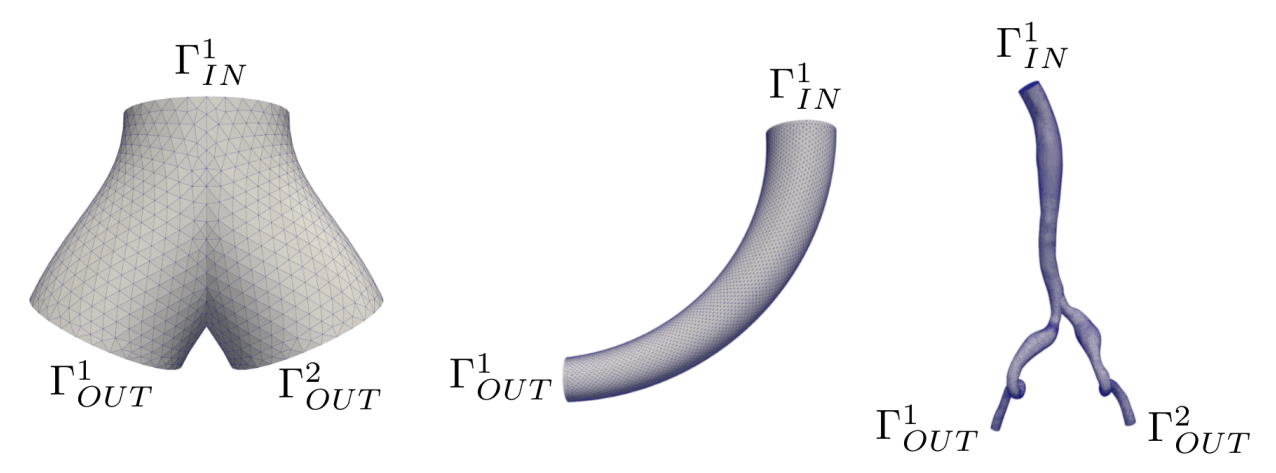


Figure 1. Geometries and computational meshes used in the three numerical experiments.

Finally, the FOM expansion $\widehat{w}^{st}(\mu^*)$ of the reduced solution $\widehat{w}(\mu^*)$ can be computed as

$$\widehat{\boldsymbol{w}}^{st}(\boldsymbol{\mu}^*) = \boldsymbol{\Phi} \ \widehat{\boldsymbol{w}}^M(\boldsymbol{\mu}^*) \ \boldsymbol{\Psi}^T \quad \in \mathbb{R}^{N^s \times N^t} \ , \tag{3.15}$$

where $\widehat{\boldsymbol{w}}^{M}(\boldsymbol{\mu}^{*}) \in \mathbb{R}^{n^{s} \times n^{t}}$ is a suitable two-dimensional reshaping of $\widehat{\boldsymbol{w}}(\boldsymbol{\mu}^{*})$, while $\boldsymbol{\Phi} \in \mathbb{R}^{N^{s} \times n^{s}}$ and $\boldsymbol{\Psi} \in \mathbb{R}^{N^{t} \times n^{t}}$ are block-diagonal matrices, whose blocks contain the velocity, pressure and Lagrange multipliers reduced bases in space and in time, respectively. Here we define $n^{s} := n^{s}_{u} + n^{s}_{p} + N_{\lambda}$ and $n^{t} := n^{t}_{u} + n^{t}_{p} + n^{t}_{\lambda}$. We remark that in Eq.(3.15) $\widehat{\boldsymbol{w}}^{st}(\boldsymbol{\mu}^{*})$ is considered a two-dimensional matrix for convenience; however, it should be conveniently flattened into a N^{st} -dimensional array to be compatible with Eq.(2.7).

4 Numerical results

In this section, we analyse the performances of the ST–GRB method on three different test cases. The "standard" RB method (denoted as SRB–TFO) serves as a baseline. All simulations were performed on the *Jed* cluster of the *Scientific IT and Application Support (SCITAS)*¹ at EPFL.

4.1 Test cases setup

We solve the unsteady incompressible Navier–Stokes equations in three–dimensional vessel anatomies. In the first test case, we neglect the effect of wall compliance, enforcing no–slip boundary conditions on the lateral wall of an idealized symmetric bifurcation geometry. In the other two test cases, instead, we focus on the physics–based reduction of the FSI problem through the coupled momentum model, considering either an elementary cylindrical geometry or the anatomy of a descending aorta with external iliac arteries [45]. The three geometries and the associated computational meshes are reported in Figure 1. In this work, we always adopt the cgs (centimeter–gram–second) unit system. So, for instance, the velocities are expressed in cm/s and the pressures in dyn/cm², where dyn := $g \cdot cm/s^2$.

We set blood density to $\rho=1.06~{\rm g/cm^3}$ and blood viscosity to $\mu=3.5\cdot 10^{-3}~{\rm g/(cm\cdot s)}$. At the inlet/outlet boundaries, depending on the test case, we either prescribe a time-varying parabolic velocity profile that matches a given volumetric flow rate or we impose homogeneous Neumann boundary conditions. As discussed in Section 2.2, Dirichlet boundary conditions on Γ_D are weakly imposed using Lagrange multipliers, whose space is discretized by orthonormal basis functions, built from Chebyshev polynomials [36]. We selected a maximal polynomial degree of 5 for the inlets, to guarantee a good approximation of the velocity profiles, and of 0 for the outlets, where we are just interested in enforcing the flow rate. More in detail, we work under the assumption that all the inlet/outlet Dirichlet boundaries $\{\Gamma_D^k\}_{k=1}^{N_D}$ are planar circular surfaces. So, let $r_k \in \mathbb{R}^+$, $c_k \in \mathbb{R}^3$, $n_k \in \mathbb{R}^3$ be the radius, the center and the outward unit normal vector of Γ_D^k , respectively. The parabolic velocity profile, that coincides with the space–dependent factor in Eq.(2.3), is then defined as follows:

$$\underline{g}_{k}^{s}(\underline{x}) := \pm \frac{2}{\pi r_{k}^{2}} \left(1 - \frac{\|\underline{x} - \boldsymbol{c_{k}}\|_{2}^{2}}{r_{k}^{2}} \right) \boldsymbol{n_{k}} \quad \text{with } \underline{x} \in \Gamma_{D}^{k} ,$$

$$(4.1)$$

¹https://www.epfl.ch/research/facilities/scitas/hardware/

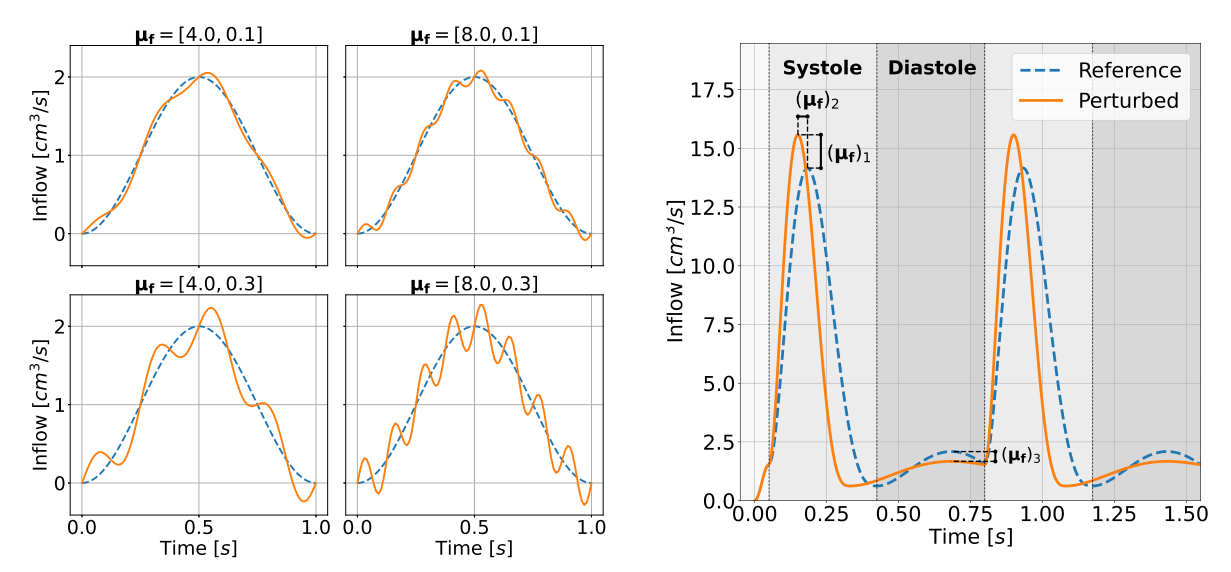


Figure 2. Volumetric blood flow waveforms considered in the three numerical experiments. In particular: (left) perturbed sinusoidal waveform, used in test cases 1 and 2; (right) parametrized supraceliac aortic waveform, obtained from patient–specific PC–MRI measurements.

where the leading sign is negative at the inlets and positive at the outlets. We remark that, since \underline{g}_k^s integrates to 1 on Γ^k_D , the term $g_t^k(t; \boldsymbol{\mu_f})$ in Eq.(2.3) coincides with the flow rate prescribed at Γ^k_D . The expressions of $\{g_t^k(t; \boldsymbol{\mu})\}_{k=1}^{N_D}$ will be defined separately for each test case.

During the offline phase, we generate a training dataset of M full-order solutions, that correspond to different parameter values $\{\mu_i\}_{i=1}^M$, sampled uniformly at random from $\mathcal{P}:=\mathcal{P}_f\times\mathcal{P}_m$. The definitions of \mathcal{P}_f (flow rate parameters space) and \mathcal{P}_m (membrane parameters space) will be detailed separately for the three test cases. The high-fidelity snapshots are computed with LifeV , a C++ FE library with support for high-performance computing [46], exploiting parallelization over 72 cores. For what concerns the discretization in space, we employ either $\mathbb{P}_2-\mathbb{P}_1$ Taylor-Hood Lagrangian finite elements (test cases 1 and 2) or $\mathbb{P}_1^b-\mathbb{P}_1$ Crouzeix-Raviart elements (test case 3) for the discretization of velocity and pressure. Time integration is performed using the implicit BDF2 method, a second-order multistep scheme with coefficients $\beta=\frac{2}{3}, \alpha_1=-\frac{4}{3}, \alpha_2=\frac{1}{3}$. The FOM sparse linear systems are solved using the preconditioned GMRES method [47], considering the saddle point block preconditioner proposed in [36]. Concerning the Newton iterations, we select a tolerance $\tau_{NR}=10^{-5}$ and a maximal number of iterations $K_{NR}=10$.

The performances of the reduced order models are assessed considering additional M^* high-fidelity simulations, corresponding to parameter values $\{\boldsymbol{\mu}_i^*\}_{i=1}^{M^*}$ that have not been used for the reduced bases generation. The accuracy of the methods is quantified by computing the average relative errors on velocity, pressure and displacement in the natural spatio-temporal norms. For $i=1,\cdots,M^*$, let $\widehat{u}_i^*\in\mathbb{R}^{n_u^{st}}$, $\widehat{p}_i^*\in\mathbb{R}^{n_p^{st}}$ be the space-time-reduced velocity and pressure obtained with ST-GRB for the parameter value $\boldsymbol{\mu}_i^*$ and let $\boldsymbol{u}_i^*\in\mathbb{R}^{N_u^{st}}$, $\boldsymbol{p}_i^*\in\mathbb{R}^{N_p^{st}}$, $\boldsymbol{d}_i^*\in\mathbb{R}^{N_d^{st}}$ denote the corresponding space-time high-fidelity solution. Here \boldsymbol{d}_i^* represents the full-order displacement field and we define $N_d^{st}:=N_d^sN^t$, where $N_d^s< N_u^s$ is the number of FOM DOFs that lie on the lateral wall Γ . Also, let $\boldsymbol{X}_u^{st}\in\mathbb{R}^{N_u^{st}\times N_u^{st}}$, $\boldsymbol{X}_p^{st}\in\mathbb{R}^{N_p^{st}\times N_p^{st}}$, $\boldsymbol{X}_d^{st}\in\mathbb{R}^{N_d^{st}\times N_d^{st}}$ be the matrices that encode the natural spatio-temporal norms for velocity, pressure and displacement, respectively. We refer to [18] for the precise definitions of \boldsymbol{X}_u^{st} and \boldsymbol{X}_p^{st} . The matrix \boldsymbol{X}_d^{st} , instead, writes as follows:

$$m{X}_d^{st} := \mathrm{diag}\Big(\underbrace{m{X}_d, \, \cdots, m{X}_d}_{N^t} \Big) \quad ext{with} \ \ m{X}_d \in \mathbb{R}^{N_d^s imes N_d^s} \ : \ \ (m{X}_d)_{ij} = \int_{\Gamma} \underline{arphi}_i^u \cdot \underline{arphi}_j^u \ .$$

	Test case		!	Tir					
Test #	Problem	Geometry	$h_{ m avg}$	N_u^s	N_p^s	N_{λ}	Δt	N^t	Duration
1	Navier-Stokes	Bifurcation	1.35 mm	76'974	3'552	66	$1.0~\mathrm{ms}$	1'000	1h 44min
2	RFSI	Tube	$2.18\;\mathrm{mm}$	86'802	4'350	63	$1.0~\mathrm{ms}$	1'000	$1h\ 47min$
3	RFSI	Aorta	$2.21\;\mathrm{mm}$	394'527	24'687	63	$1.0\ \mathrm{ms}$	1'550	$10 \mathrm{h}\ 24 \mathrm{min}$

Table 1. Average mesh size (h_{avg}), timestep size, number of space and time FOM DOFs for velocity, pressure and Lagrange multipliers, and average duration of a FOM simulation (on 72 cores) in the three test cases.

			В	ases cor	struction				
Test #	M	Method	$oldsymbol{u}$		$oldsymbol{p}$		Assembling		
			Space	Time	Space	Time	IG	Conv (n _c)	Other
1	50	SRB-TFO ST-GRB	550 s	// 1 s	20 s	// ; 1 s	// 38 s	231 s ⁽³⁹⁾	2 s 2 s
2	50	SRB-TFO ST-GRB	547 s	// 1 s	37 s	// ; 1 s	// 32 s	65 s (10)	3 s 3 s
3	25	SRB-TFO ST-GRB	497 s	// 6 s	75 s	// ; 1 s	// 162 s	2'928 s ⁽⁹³⁾	9 s 12 s

Table 2. Offline computational costs, expressed in terms of CPU-time (in s), in the three test cases, for $\varepsilon_u=\varepsilon_p=\varepsilon_\lambda^t=10^{-3}$ and $\varepsilon_\lambda^s=10^{-5}$.

The average relative errors are then

$$E_{u} = \frac{1}{M^{*}} \sum_{i=1}^{M^{*}} \frac{\|\mathbf{\Pi}^{u} \widehat{\boldsymbol{u}}_{i}^{*} - \boldsymbol{u}_{i}^{*} \|_{\boldsymbol{X}_{u}^{st}}}{\|\boldsymbol{u}_{i}^{*} \|_{\boldsymbol{X}_{u}^{st}}}; \quad E_{p} = \frac{1}{M^{*}} \sum_{i=1}^{M^{*}} \frac{\|\mathbf{\Pi}^{p} \widehat{\boldsymbol{p}}_{i}^{*} - \boldsymbol{p}_{i}^{*} \|_{\boldsymbol{X}_{p}^{st}}}{\|\boldsymbol{p}_{i}^{*} \|_{\boldsymbol{X}_{p}^{st}}}; \quad E_{d} = \frac{1}{M^{*}} \sum_{i=1}^{M^{*}} \frac{\|\mathbf{\Pi}^{d} \widehat{\boldsymbol{u}}_{i}^{*} - \boldsymbol{d}_{i}^{*} \|_{\boldsymbol{X}_{d}^{st}}}{\|\boldsymbol{d}_{i}^{*} \|_{\boldsymbol{X}_{d}^{st}}}.$$

$$(4.2)$$

To guarantee a fair comparison of the performances across different choices of the tolerances in the truncated POD algorithm, we express accuracy by means of the ratios E_u/ε_u , E_p/ε_p , E_d/ε_u , where ε_u , $\varepsilon_p \in \mathbb{R}^+$ are the user-defined POD tolerances for velocity and pressure (in both space and time), respectively. In the following, we will refer to such quantities as the normalized average relative errors. Incidentally, we define ε_λ^s , $\varepsilon_\lambda^t \in \mathbb{R}^+$ as the POD tolerances for the Lagrange multipliers, respectively, in space and in time. To quantify the computational efficiency, instead, we consider two different indicators: the speedup (SU), defined as the ratio between the average duration of FOM and ROM simulations, and the reduction factor (RF), computed as the ratio between the number of FOM and ROM DOFs.

Table 1 reports the average mesh size, the timestep size, the number of FOM DOFs in space and in time and the average duration of a single high-fidelity simulation (performed in parallel over 72 cores) for the three test cases. By comparing test cases 1 and 2, that feature a similar number of DOFs, we remark that the use of the coupled momentum model — denoted for convenience as RFSI — does not entail important increases in the computational cost.

Table 2 summarizes the offline costs of SRB-TFO and ST-GRB, using a POD tolerance of $\varepsilon=10^{-3}$ for all the fields, both in space and in time. Three remarks are worth to follow. Firstly, as also observed in [18], all the wall-times reported in Table 2 are a small fraction of a single FOM solve. This reveals that the high-fidelity data generation (or availability) is the true bottleneck of the offline phase. Neglecting the construction of the FOM solutions cohort, the computation of the velocity reduced basis in space appears as the most expensive offline operation, with a duration of roughly 10 min for all the test cases. Nonetheless, we remark that assembling the affine components for the convective term and its jacobian (see Section 3.3.2) also entails an important cost. The associated wall-time is reported in the column Conv, considering n_c equal to the number of velocity basis functions prior to the supremizers' enrichment; such value is reported as a superscript. Notably, the affine components assembly takes approximately six times longer than the reduced bases generation for the aorta test case. However, it is worth mentioning that parallelization was

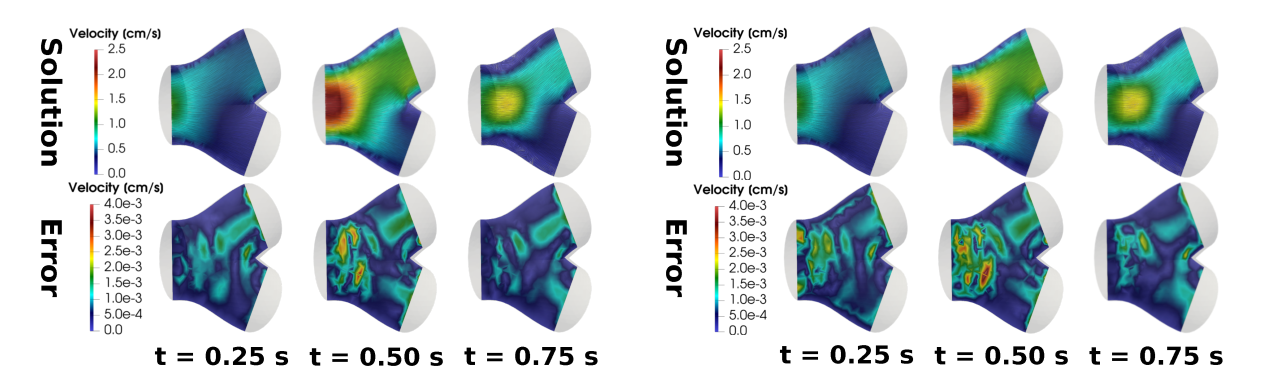


Figure 3. Line integral convolution of the velocity field on the median slice (top) and corresponding pointwise absolute error (bottom) at three time instants, obtained with SRB-TFO (left) and ST-GRB right for $\mu_f^* = [7.56, 0.14, 0.74]$.

not exploited at this stage, despite the task at hand being embarrassingly parallelizable. Compared to SRB-TFO, the computational cost of ST-GRB is increased by the use of interpolation-based techniques to determine a good initial guess for the Newton iterations. Indeed, this step requires the offline projection of the spatio-temporal FOM snapshots onto the reduced subspace. This operation carries a non-negligible computational burden (see column *IG*), that scales linearly with the number of snapshots *M*. Lastly, we underline that the offline cost of model order reduction in space is largely dominant not only for the reduced bases generation, but also for the assembling of parameter-independent quantities (see Section 3.3.1); the associated wall-time is reported in the column *Other*. In fact, the offline assembling phase of ST-GRB is substantially as expensive as the one of SRB-TFO, for all the test cases. As a result, the calculation of the generalized coordinates of the FOM snapshots configures as the primary differentiating factor in efficiency between the offline phases of SRB-TFO and ST-GRB.

4.2 Test case 1: rigid Navier–Stokes in a symmetric bifurcation

We investigate the performances of ST–GRB in solving the Navier–Stokes equations in an idealized symmetric bifurcation geometry (see Figure 1 – left). At the inlet $\Gamma^1_{\rm IN}$, we impose a parabolic velocity profile (see Eq.(4.1)) that matches the following parametrized volumetric flow rate (see Figure 2 – left):

$$g_1^t(t; \boldsymbol{\mu_f}) = 1 - \cos\left(\frac{2\pi t}{T}\right) + (\boldsymbol{\mu_f})_2 \sin\left(\frac{2\pi(\boldsymbol{\mu_f})_1 t}{T}\right), \tag{4.3}$$

where T=1 s is the final time of the simulation. To enhance variability within the solution manifold, we unbalance the flow in the two outlet branches by (weakly) enforcing the outflow rate $g_2^t(t; \boldsymbol{\mu_f}) := (\boldsymbol{\mu_f})_3 \ g_1^t(t; \boldsymbol{\mu_f})$ on Γ_{OUT}^1 . Hence, we have that $\boldsymbol{\mu_f} \in \mathbb{R}^3$; we define the space of flow rate parameters as $\mathcal{P}_f = [4.0, 8.0] \times [0.1, 0.3] \times [0.2, 0.8]$. On Γ_{OUT}^2 we impose homogeneous Neumann boundary conditions. We underline that in this test case we neglect wall compliance; so, $\mathcal{P}_m = \emptyset$ and no–slip boundary conditions are strongly enforced at the lateral wall Γ . Unless otherwise specified, in the numerical tests we choose the POD tolerances $\varepsilon_u = \varepsilon_p = \varepsilon_\lambda^t = 10^{-3}, \ \varepsilon_\lambda^s = 10^{-5}, \ n_{c,J} = 0$ affine components for the Jacobian of the convective term, and we compute the initial guess $\widehat{\boldsymbol{w}}^{(0)}$ through PODI (see Eq.(3.14)).

Figure 3 shows the line integral convolution of the velocity field on the median slice of the domain obtained for $\mu_f^* = [7.56, 0.14, 0.74]$ with SRB-TFO and ST-GRB, and the corresponding pointwise error with respect to the FOM solution. We underline that this parameter value was not considered to generate the reduced basis during the offline phase of the method. The velocity relative errors (see Eq.(4.2)) for this particular experiment are 0.28% for SRB-TFO and 0.61% for ST-GRB. From a qualitative standpoint, the two solutions are almost undistinguishable at the three displayed time instants. Notably, both SRB-TFO and ST-GRB are able to capture the flow recirculation phenomenon that occurs after the flow peak, during the deceleration phase.

Figure 4 shows the trend of the normalized average relative test errors and of the computational wall times with respect to the number of affine components n_c , considered for the approximation of the convective term (see Eq.(3.10)). Both SRB-TFO and ST-GRB exhibit a decreasing error trend for small values of n_c , while a plateau is reached once a sufficiently large number of convective modes is included. On the one side, this behaviour tells that an imprecise

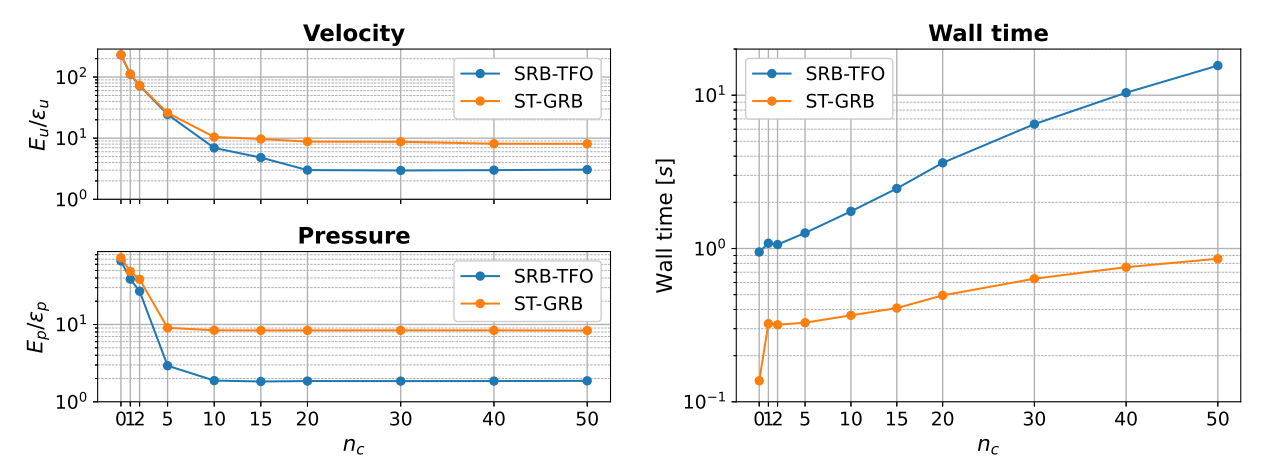


Figure 4. Trend of velocity and pressure normalized average test relative errors (left) and speedups (right) with respect to n_c , the number of affine components for the nonlinear reduced convective term.

approximation of the nonlinearity severely deteriorates the solution quality. However, on the other side, it also highlights that good quality solutions can be obtained considering a relatively small number of affine components. More in detail, we notice that SRB–TFO is always more accurate than ST–GRB, and that the plateau in the error is reached later with SRB–TFO and for the velocity field. These behaviours can be explained considering that ST–GRB introduces an additional reduction layer compared to SRB–TFO and that the definition of the convective term does not explicitly depend on pressure. Concerning efficiency, we observe that the wall–time is strongly related to n_c with SRB–TFO, while such dependency is weaker with ST–GRB. This result can be justified considering the impact of the convective term assembly on the overall online phase duration. Indeed, with ST–GRB, the most expensive online operation consists in solving dense linear systems of dimension $n^{st} \approx 10^3$, and assembling the convective term (once per Newton iteration) carries a smaller cost, at least for sufficiently small values of n_c . Conversely, with SRB–TFO, the nonlinear term assembly cost (once per Newton iteration at every timestep) eclipses the one of solving dense linear systems of dimension $n^s \approx 10^2$, which explains the observed markedly increasing wall–time trend. Ultimately, the value $n_c = 20$ appears to provide the best trade–off between accuracy and efficiency for both methods. Therefore, we used it in all the numerical experiments reported for this test case.

As pointed out in Section 3.4, the choice of the initial guess for the Newton iterations is not straightforward in the context of space-time model order reduction. For this reason, we investigate six different alternatives. The results of the numerical tests, conducted both neglecting and including the convective Jacobian modes, are summarized in Table 3, and demonstrate that ST-GRB benefits from a smart choice of the initial guess. Indeed, naively selecting $\widehat{w}^{(0)} = \mathbf{0}$ (Zero) yields rather imprecise approximations, particularly for the velocity field. Conversely, fast convergence and accurate solutions are attained when employing non-intrusive ROMs, such as K-NN (with K = 1, 3, 5) and PODI. In particular, for both $n_{c,J} = 0$ and $n_{c,J} = 20$, the best results are obtained with PODI, even though 3-NN also showcases similar performances. Three remarks are worth following. Firstly, selecting $\widehat{w}^{(0)} = \frac{1}{M} \sum_{i=1}^{M} \widehat{w}(\mu_i)$ (Average) leads to convergent Newton iterations and low errors (at least for $n_{c,J} = 20$), despite this choice is not tailored to the value of μ^* . Secondly, taking into account the convective Jacobian modes enhances accuracy at the cost of larger computational times, even if the average number of Newton iterations is lowered. In this regard, we underline that LU factorization of the left-hand side matrix was not exploited in these tests, to guarantee a fair comparison of the different alternatives. Finally, we note that both the number of Newton iterations and the online times—to—solution are similar for all the considered initial guesses, except for the case $\widehat{w}^{(0)} = \mathbf{0}$ with $n_{c,J} = 0$. This result indicates that the online query of the non-intrusive ROMs entails negligible computational costs.

In Table 4, we report the reduced bases sizes and the performance metrics of SRB-TFO and ST-GRB, considering four different POD tolerances. From a general standpoint, model order reduction in time makes ST-GRB more efficient, but less accurate than SRB-TFO. For instance, in the case of $\varepsilon=10^{-3}$, ST-GRB is roughly 10 times faster than SRB-TFO (average simulation duration: $0.38~{\rm s}$ vs. $4.04~{\rm s}$), but its errors are approximately 3 times larger for the velocity and 4 for the pressure. Nonetheless, the computational advantages of ST-GRB vanish as smaller values of ε are considered. In fact, for $\varepsilon=10^{-4}$, SRB-TFO is not just more accurate but also faster than ST-GRB (average simulation duration: $4.46~{\rm s}$ vs. $6.94~{\rm s}$). This behaviour is mainly related to the computational cost of solving linear

	Zero		Average		1-NN		3-NN		5-NN		PODI	
$n_{c,J}$	0	20	0	20	0	20	0	20	0	20	0	20
$E_u/arepsilon_u$	40.6	23.2	9.82	8.23	9.15	8.22	8.81	8.21	8.99	8.21	8.78	8.20
$E_p/arepsilon_p$	8.47	10.1	8.37	8.43	8.36	8.41	8.38	8.40	8.37	8.40	8.39	8.39
$\overline{E_u^{(0)}/arepsilon_u}$	$E_u^{(0)}/\varepsilon_u$ 1000		294		179		161		174		146	
$E_p^{(0)}/arepsilon_p$	10	00	73	38	6	10	58	88	60	03	59	99
Iterations	7	2.2	3.8	2.1	3.6	2.1	3.6	2	3.6	2	3.5	2
Time [s]	0.85	1.13	0.48	1.25	0.47	1.27	0.49	1.14	0.53	0.94	0.50	1.03

Table 3. Normalized average relative test errors on the solution and on the initial guess, average number of Newton iterations and wall times. The results have been obtained considering the ST–GRB method with different choices of the initial guess in the Newton iterations and different numbers of affine components for the convective Jacobian. The quantities $E_u^{(0)}$, $E_p^{(0)}$ denote the average relative test error on velocity and pressure, considering the initial guess as reduced solution.

			ROM	size	Effic	iency	Accuracy		
	ε	$\overline{(n_u^s,n_u^t)}$	(n_p^s, n_p^t)	$\overline{(\{N_{\lambda_k}\},\{n^t_{\lambda_k}\})}$	RF	SU	$\overline{E_u/arepsilon_u}$	$E_p/arepsilon_p$	
0	5e-3	$(41, \cdot)$	$(4, \cdot)$	$\{(15,\cdot),(2,\cdot)\}$	1.30e3	2.05e3	5.87	1.17	
ŦŦ	1e-3	$(74, \cdot)$	$(9,\cdot)$	$\{(23,\cdot),(3,\cdot)\}$	7.39e2	1.66e3	3.01	1.85	
SRB-TFO	5e-4	$(93, \cdot)$	$(12, \cdot)$	$\{(27,\cdot),(3,\cdot)\}$	5.97e2	1.54e3	2.87	1.54	
SK	1e-4	$(159, \cdot)$	$(21, \cdot)$	$\{(41,\cdot),(3,\cdot)\}$	3.60e2	1.39e3	11.3	1.97	
- 8	5e-3	(41,16)	(4,13)	{(15,14), (2,12)}	8.55e4	4.20e4	18.4	16.3	
2	1e-3	(74,21)	(9,19)	{(23,19), (3,15)}	3.65e4	1.62e4	8.78	8.39	
ST-GRB	5e-4	(93,23)	(12,21)	{(27,22), (3,15)}	2.66e4	4.94e3	8.76	5.51	
S	1e-4	(159,33)	(21,32)	$\{(41,32), (3,21)\}$	1.10e4	8.96e2	32.4	13.7	

Table 4. Results obtained with SRB–TFO and ST–GRB on the Navier–Stokes symmetric bifurcation test case, for different POD tolerances ε . In particular: (left) size of the spatial and temporal reduced bases for velocity, pressure and Lagrange multipliers; (center) reduction factor and average speedup; (right) normalized average relative test errors on velocity and pressure.

systems. Indeed, solving a single n^{st} -dimensional (with $n^{st}=n^sn^t$) dense linear system is cheaper than sequentially solving N^t distinct n^s -dimensional dense linear systems only if $n^t \ll N^t$. Since direct linear systems solvers have at most a cost of $\mathcal{O}(N^3)$, we can claim that ST-GRB is cheaper than SRB-TFO if $n^t \lesssim \sqrt[3]{N^t}$. For this particular test case, where $N^t=10^3$, computational gains are realized up to $n^t\approx 20$ temporal reduced bases, which corresponds to setting $\varepsilon=5\cdot 10^{-4}$. Lastly, we highlight that the results reported in Table 4 have been obtained for $n_{c,J}=0$, i.e. neglecting the presence of the convective Jacobian in the Newton iterations. This implies that the left-hand side matrix of the linear systems to be solved is parameter-independent, since the flow rate parametrization solely affects the right-hand side vector. Therefore, a pre-computed LU factorization can be exploited to further boost the efficiency of both methods, at no loss in accuracy. Remarkably, the computational gains stemming from this strategy are more important, in relative terms, with ST-GRB than with SRB-TFO, because larger linear systems are solved under space-time model order reduction. For example, in the case of $\varepsilon=10^{-3}$, leveraging LU decomposition allows to lower the average simulation duration of 19% with SRB-TFO (from 4.04 s to 3.26 s) and of 66% with ST-GRB (from 0.38 s to 0.13 s).

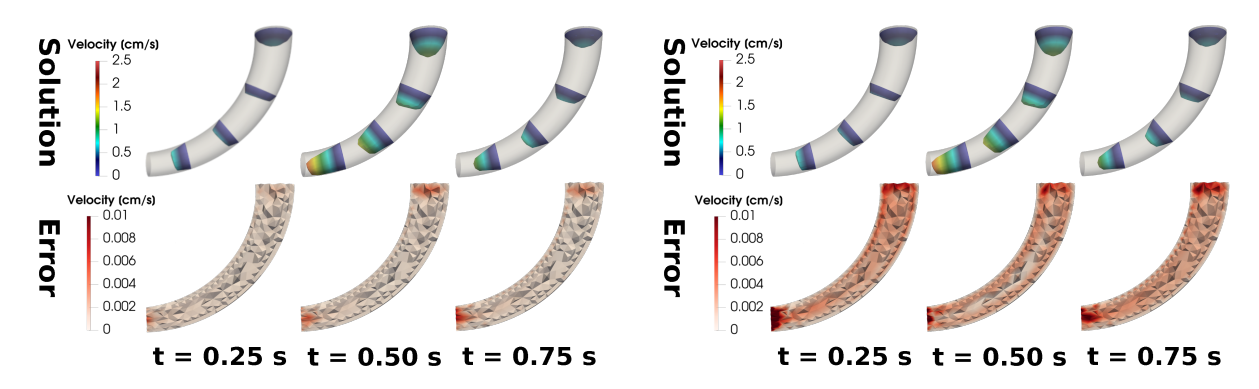


Figure 5. Velocity field at 4 different slices along the vessel centerline (top) and pointwise absolute error on the median slice (bottom) at three time instants, obtained with SRB-TFO (left) and ST-GRB (right) for $\mu^* = [0.12, 1.44, 5.20 \cdot 10^6, 0.36]$.

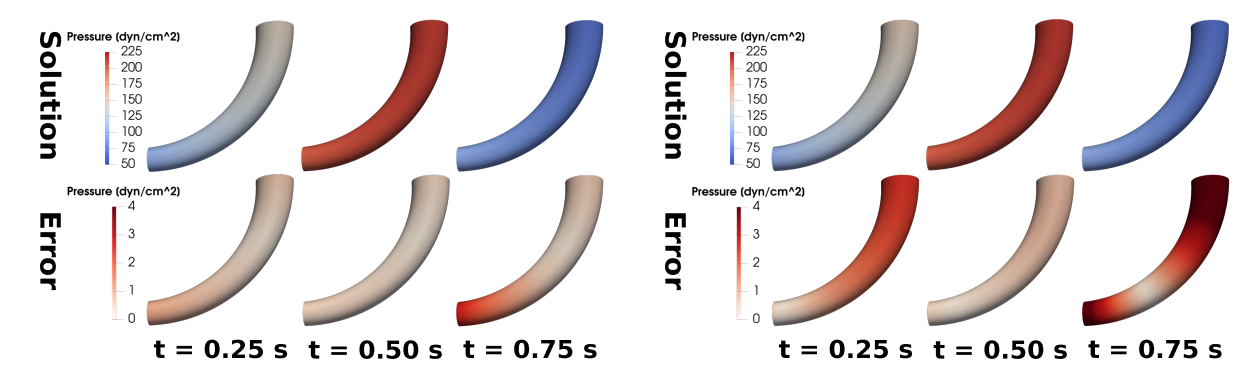


Figure 6. Pressure field (top) and corresponding pointwise absolute error (bottom) at three time instants, obtained with SRB-TFO (left) and ST-GRB (right) for $\mu^* = [0.12, 1.44, 5.20 \cdot 10^6, 0.36]$.

4.3 Test case 2: Coupled Momentum model in a bent tube

In this test case, we numerically investigate the application of ST–GRB to the reduced FSI problem which stems from the use of the coupled momentum model to account for the vessel wall compliance. We consider a bent tube geometry, featuring a diameter–length aspect ratio of 1:4 (see Figure 1 – middle). We avoid the flow rate variability (hence $\mathcal{P}_f = \emptyset$), so that the problem parametrization entirely depends on the vessel wall properties and it is affine. The space of membrane parameters, whose generic element is $\mu_m = [h_s, \rho_s, E, \nu]$, is defined as $\mathcal{P}_m := [0.05, 0.15] \times [1.08, 1.80] \times [2 \cdot 10^6, 6 \cdot 10^6] \times [0.35, 0.5] \subset \mathbb{R}^4$. Also, we do not take into account the elastic response of the surrounding tissues, thus setting $c_s = 0$ (see Eq.(2.6)). At the inlet Γ^1_{IN} , we (weakly) prescribe a parabolic velocity profile that matches the flow rate $g^t = g_1^t(\cdot;\mathbf{0})$, where g_1^t is defined as in Eq.(4.3). At the outlet Γ^1_{OUT} we impose absorbing boundary conditions, with a resistance $R = 100~\mathrm{g}\ /(\mathrm{cm}^4 \cdot \mathrm{s})$. Furthermore, we enforce the following boundary conditions at the inlet/outlet rings:

$$\underline{u} \cdot \boldsymbol{n}_{\text{IN}} = 0; \quad \boldsymbol{n}_{\text{IN}}^T \sigma(\underline{u}, p) (I - \boldsymbol{n}_{\text{IN}} \otimes \boldsymbol{n}_{\text{IN}}) = \underline{0}; \quad \text{on } \Gamma_{\text{IN}}^{1,r} := \Gamma \cap \Gamma_{\text{IN}}^1;
\underline{u} \cdot \boldsymbol{n}_{\text{OUT}} = 0; \quad \boldsymbol{n}_{\text{OUT}}^T \sigma(\underline{u}, p) (I - \boldsymbol{n}_{\text{OUT}} \otimes \boldsymbol{n}_{\text{OUT}}) = \underline{0}; \quad \text{on } \Gamma_{\text{OUT}}^{1,r} := \Gamma \cap \Gamma_{\text{OUT}}^1;$$
(4.4)

where $n_{\rm IN}, n_{\rm OUT} \in \mathbb{R}^3$ are the outward unit normal vectors to $\Gamma^1_{\rm IN}, \Gamma^1_{\rm OUT}$, respectively. Eq.(4.4) enables tangential deformations of the inlet/outlet faces, while it prevents any displacement in the normal direction. Unless otherwise specified, in the following tests we consider $\varepsilon_u = \varepsilon_p = \varepsilon_\lambda^t = 10^{-3}, \ \varepsilon_\lambda^s = 10^{-5}$ as POD tolerances, $n_{c,J} = 0$ affine components for the Jacobian of the convective term, and an initial guess $\widehat{w}^{(0)}$ that is computed with the PODI approach. Furthermore, we select n_c as the number of velocity modes obtained after the truncated POD in space, thus neglecting the supremizers when computing the affine approximation of the convective term.

Figures 5, 6 show, respectively, the velocity and the pressure field at three equispaced time instants obtained with SRB-TFO and ST-GRB for $\mu^* = [0.12, 1.44, 5.20 \cdot 10^6, 0.36]$, and the corresponding pointwise absolute errors with

			ROM si		Effic	iency	Accuracy			
	ε	$\overline{(n_u^s,n_u^t)}$	(n_p^s, n_p^t)	$(n_\lambda^s, n_\lambda^t)$	n_c	RF	SU	$\overline{E_u/arepsilon_u}$	$E_p/arepsilon_p$	$E_d/arepsilon_u$
	1e-2	$(10, \cdot)$	$(2, \cdot)$	$(3, \cdot)$	5	6.08e3	4.06e3	4.97	26.6	6.02
F	5e-3	$(12, \cdot)$	$(2, \cdot)$	$(4, \cdot)$	6	5.07e3	3.86e3	9.72	39.5	9.04
SRB-TFO	1e-3	$(17, \cdot)$	$(2, \cdot)$	$(5,\cdot)$	10	3.80e3	2.58e3	4.65	5.80	9.96
Z.	5e-4	$(20,\cdot)$	$(2, \cdot)$	$(6, \cdot)$	12	3.26e3	2.92e3	10.9	11.6	17.3
9 2	1e-4	$(32, \cdot)$	$(4, \cdot)$	$(8, \cdot)$	20	2.07e3	1.75e3	21.6	24.0	9.65
	1e-2	(10,3)	(2,2)	(3,2)	5	2.28e6	2.44e6	6.00	12.9	6.23
SB B	5e-3	(12,3)	(2,2)	(4,2)	6	1.90e6	1.96e6	9.63	24.1	9.94
ST-GRB	1e-3	(17,7)	(2,3)	(5,4)	10	6.29e5	3.82e5	13.3	26.4	14.7
ST-	5e-4	(20,9)	(2,5)	(6,5)	12	4.15e5	5.41e5	20.4	42.8	21.4
	1e-4	(32,22)	(4,9)	(8,9)	20	1.12e5	1.10e5	23.8	31.2	9.88

Table 5. Results obtained with SRB–TFO and ST–GRB on the coupled momentum bent tube test case, for different POD tolerances ε . In particular: (left) size of the spatial and temporal reduced bases for velocity, pressure and Lagrange multipliers, and number of affine components for the reduced convective term; (center) reduction factor and average speedup; (right) normalized average relative test errors on velocity, pressure and displacement.

respect to the FOM solution. This parameter was not considered for the computation of the reduced bases during the offline phase. The relative errors, measured in the natural spatio–temporal norms, for this particular test case are: 0.50% for the velocity, 0.58% for the pressure, 1.33% for the displacement with SRB–TFO; 1.26% for the velocity, 2.51% for the pressure, 1.73% for the displacement with ST–GRB. From a qualitative standpoint, we remark that the solution approximations yielded by the two methods are substantially indistinguishable by the eye. Nonetheless, as pointed out in Section 4.2, we recognize that SRB–TFO attains better accuracy levels, since the temporal dynamics are processed in a high–fidelity fashion. For what concerns the velocity field, in particular, we notice larger errors close to the extremal boundaries. In the outlet region, this behaviour could be expected, since the flow is accelerated by the vessel lumen narrowing. At the inlet, instead, large errors can be linked to the weak imposition of the Dirichlet boundary conditions; in fact, the normalized relative errors on the Lagrange multipliers are relatively high both with SRB–TFO (4.04%) and with ST–GRB (4.33%).

Table 5 reports the reduced bases sizes, the number of convective affine components and the performance metrics of SRB-TFO and ST-GRB for five different POD tolerances. From a general perspective, we observe that ST-GRB yields slightly less accurate results than SRB-TFO, but at a significantly lower computational cost. This suggests that the additional reduction layer introduced by temporal dynamics compression does not compromise approximation quality, while substantially enhancing efficiency. In fact, the advantages of ST-GRB over SRB-TFO are more pronounced compared to the first test case, because the temporal reduced basis sizes are smaller. This is primarily due to the imposition of a non-perturbed inflow rate and to the simpler domain topology. Furthermore, absorbing boundary conditions at the outlet prevent the onset of non-physiological reflecting waves. From a quantitative standpoint, we note that both velocity and pressure errors are roughly one order of magnitude larger than the prescribed POD tolerance. Remarkably, the same consideration holds also for the displacement field, even if its values are roughly three orders of magnitude smaller than the velocity ones. Incidentally, we underline that the larger errors made by ST-GRB can be justified taking into account both the temporal dynamics compression and the different treatment of the structural displacement. Indeed, high-fidelity-in-time approaches, such as the FOM and SRB-TFO, feature an explicit embedding of the displacement dynamics within the Navier-Stokes equations, based on the kinematic coupling condition. Conversely, our implementation of ST-GRB implicitly encapsulates the wall mechanics into the fluid's equations (see Eq.(3.1)). For what concerns computational efficiency, we highlight that ST-GRB is much faster than SRB-TFO for all the considered POD tolerances, even though its gains shrink as higher precision results are sought. For instance, ST–GRB is 600 times faster than SRB–TFO for $\varepsilon=10^{-2}$ (2.64 ms vs. 1.57 s), 150 times faster for $\varepsilon=10^{-3}$ (16.9 ms vs. 2.50 s), and "only" 60 times faster for $\varepsilon=10^{-4}$ (58.5 ms vs. 3.68 s). Lastly, we highlight that considering the (approximate) convective term Jacobian in the Newton iterations does not substantially improve accuracy, while it moderately dilutes the computational gains. For example, if we employ ST-GRB and we set $\varepsilon = 10^{-3}$ and $n_{c,J} = 10$, the normalized average relative test errors on velocity and pressure decrease, respectively, of 2.40% (from 13.3 to 13.0) and 0.08% (from 26.4 to 26.3), while the average online time-to-solution increases of 32.2% (from 1.14 ms to 1.69 ms).

			ROM size	:	Efficiency	Accuracy			
	arepsilon	$\overline{(n_u^s,n_u^t)}$	(n_p^s, n_p^t)	$(n_{\lambda}^s,n_{\lambda}^t)$	Duration	E_u	E_p	E_d	
	1e-2	(39, ·)	$(2, \cdot)$	$(2, \cdot)$	13.1 s	6.13%	1.98%	1.41%	
SRB-TFO	5e-3	$(61, \cdot)$	$(3, \cdot)$	$(3, \cdot)$	$12.2 \mathrm{\ s}$	3.25%	0.47%	0.91%	
	1e-3	(108, ·)	(6, ·)	(9, ·)	14.1 s	2.40%	0.10%	0.29%	
	1e-2	(39, 32)	(2, 6)	(2, 3)	0.27 s	15.5%	3.14%	4.91%	
ST-GRB	5e-3	(61, 44)	(3, 8)	(3, 5)	$0.50 \mathrm{\ s}$	7.96%	1.64%	6.66%	
	1e-3	(108, 79)	(6, 19)	(9, 9)	$6.76 \mathrm{\ s}$	3.84%	0.48%	0.98%	

Table 6. Results obtained with SRB–TFO and ST–GRB on the coupled momentum aorta test case. In particular: (left) size of the spatial and temporal reduced bases for velocity, pressure and Lagrange multipliers; (center) average duration; (right) average relative test errors on velocity, pressure and displacement.

4.4 Test case 3: Coupled Momentum model in aorta and iliac arteries

This last numerical experiment analyses the application of ST-GRB in a realistic scenario. We consider the physiological geometry of an aorta with left and right external iliac arteries [45] (see Figure 1 – right). At the inlet, we weakly enforce a parabolic velocity profile that matches a patient-specific supraceliac blood flow waveform, measured from PC-MRI and spanning over two heartbeats (see Figure 2 - right). In fact, we enhance the solution manifold variability by parametrizing the available measurements. Specifically, we introduce three parameters that characterize the systolic flow peak, the time-to-peak-systole and the diastolic flow peak, and the space of flow parameters is defined as $\mathcal{P}_f = [12.0, 16.3] \times [0.11, 0.16] \times [1.57, 2.62] \subset \mathbb{R}^3$. The space of membrane parameters, whose generic element is $\mu_m = [h_s, \rho_s, E, \nu]$, is defined as $\mathcal{P}_m := [0.075, 0.125] \times [1.08, 1.50] \times [3 \cdot 10^6, 5 \cdot 10^6] \times [0.4, 0.5] \subset \mathbb{R}^4$. Following [48, 28], we account for the constraint of the surrounding tissues and set $c_s = 6 \cdot 10^4 \text{ dyn/cm}^3$. At the two outlets, we impose equivalent resistance boundary conditions, setting $R=1.6\cdot 10^4~{\rm g}~/({\rm cm}^4\cdot {\rm s})$. This value was taken from a SimVascular [49] tutorial ² conducted on the same geometry (albeit featuring more downstream branches), and it was computed from subject-specific flow rate measurements. Additionally, we simply enforce zero velocity at the inlet/outlet rings. For what concerns the ROM simulations, we always consider a space POD tolerance on Lagrange multipliers that is two orders of magnitude lower than the other tolerances. Preliminary tests — analogous to the ones performed in Section 4.2 — suggested that considering $n_c = 15$ convective affine components provides the best trade-off between accuracy and efficiency; also, we neglect the convective Jacobian affine components in this test case. Finally, with ST-GRB, we compute the initial guess using the PODI approach.

Table 6 reports the reduced basis sizes and the performance metrics of SRB–TFO and ST–GRB, considering three different POD tolerances. The outcomes are similar to the ones discussed in Section 4.3 for the tube test case. In particular, for any fixed POD tolerance ε , ST–GRB is less accurate than SRB–TFO; for instance, the velocity error is roughly doubled in all cases. However, ST–GRB is always much faster than SRB–TFO and its computational gains get amplified at large values of ε . We highlight that the average online time–to–solution of ST–GRB simulations features a much stronger dependency on the POD tolerance than the one of SRB–TFO. Ultimately, it is possible to claim that ST–GRB outperforms SRB–TFO on the test case at hand. Indeed, by comparing the results of SRB–TFO for $\varepsilon = 5 \cdot 10^{-3}$ and of ST–GRB for $\varepsilon = 10^{-3}$, we observe similar relative errors, but ST–GRB is almost two times faster (6.76 s vs. 12.2 s).

Figure 7 shows the velocity and pressure fields at systole and diastole of the second heartbeat, obtained with SRB-TFO and ST-GRB for $\varepsilon=10^{-3},~\mu_f^*=[0.11,13.2,2.40],~\mu_m^*=[0.097,1.50,3.07\cdot10^6,0.43];$ the corresponding pointwise errors with respect to the FOM solution are also represented. The relative errors in the natural spatio-temporal norms for this test case are: 2.53% for the velocity, 0.11% for the pressure and 0.28% for the displacement with SRB-TFO; 4.24% for the velocity, 0.43% for the pressure and 1.00% for the displacement with ST-GRB. For what concerns velocity, the largest errors are observed, at both timesteps, at the inlet and in the regions where complex flow patterns arise, namely the bifurcation and the final portion of the common iliac trunk. From a qualitative standpoint, the enhanced accuracy carried by SRB-TFO is nearly invisible by the eye, at the cost of more important computational costs. Regarding pressure, instead, both methods are extremely accurate, attaining

²https://simvascular.github.io/clinical/aortofemoral1.html

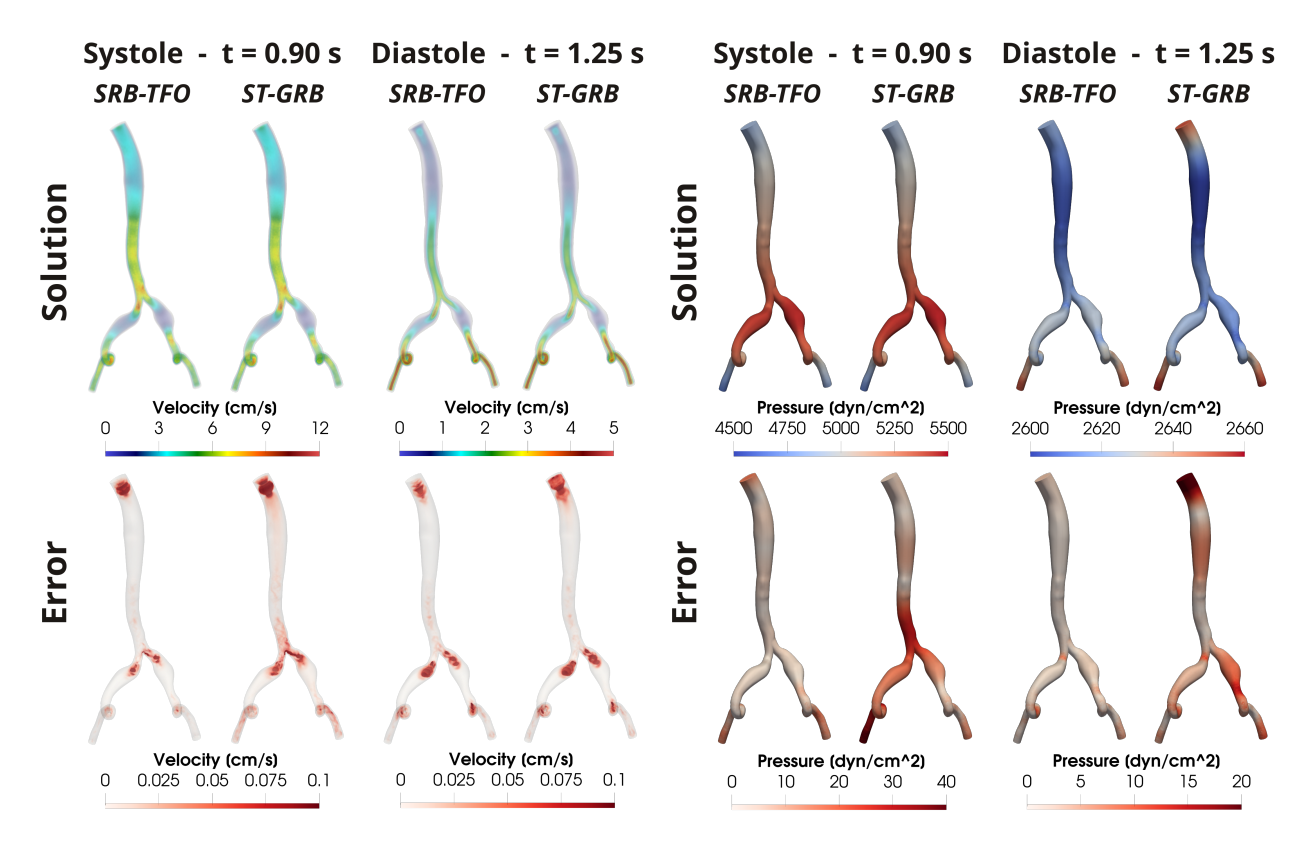


Figure 7. Systolic and diastolic velocity (left) and pressure (right) solutions (top) and errors (bottom), obtained with SRB-TFO and ST-GRB for $\varepsilon=10^{-3}$, $\boldsymbol{\mu_f^*}=[0.11,13.2,2.40]$, $\boldsymbol{\mu_m^*}=[0.097,1.50,3.07\cdot10^6,0.43]$.

accuracies aligned with the prescribed POD tolerance. Nonetheless, the higher precision level of SRB-TFO is more evident, as ST-RB produces relatively large errors in the bifurcation region during systole and at the inlet during diastole.

Finally, Figure 8 reports the approximation results for the wall shear stress (WSS) — the frictional force exerted by blood on the endothelium — obtained with both SRB-TFO and ST-GRB. In particular, on the right we report the spatial distribution of three aggregated-in-time WSS-based quantities, namely the time averaged WSS (TAWSS), the oscillatory shear index (OSI) [50] and the topological shear variation index (TSVI) [51, 52]. We remark that these quantities were found to be reliable predictors of atherosclerotic plaques growth and, in coronary arteries, of myocardial infarction [53, 54]. Notably, SRB-TFO and ST-GRB produce very similar results, which implies that the compression of the temporal dynamics does not affect accuracy on aggregated-in-time indicators. Incidentally, it is work underlining that taking into account vessel wall elasticity is crucial for accurately simulating the evolution of WSS over time; however, time-averaged indicators can be precisely identified also under the rigid wall assumption [55]. On the left, instead, we report the space-averaged WSS over time, computed over two conveniently located portions of the vessel wall. While the results attained with SRB-TFO are closer to the high-fidelity target, particularly on *Region A*, ST-GRB is nonetheless able to nicely capture the macroscopic trends.

5 Conclusions

In this work, we discussed the application of the ST-GRB method for the efficient numerical simulation of hæmodynamics in compliant vessels. We considered three-dimensional vascular anatomies (either idealized or realistic) and exploited linear projections onto *ad hoc* low-dimensional spatio-temporal subspaces to effectively solve the unsteady incompressible Navier-Stokes equations. Relying on the coupled momentum model, the latter have been endowed with non-standard Robin boundary conditions, that seamlessly allow to take into account the effect of wall compliance on the flow. Therefore, compared to classical CFD solvers, the proposed model is characterized by reduction processes that happen both at the physical and at the numerical level. To the best of our knowledge, this work represents the

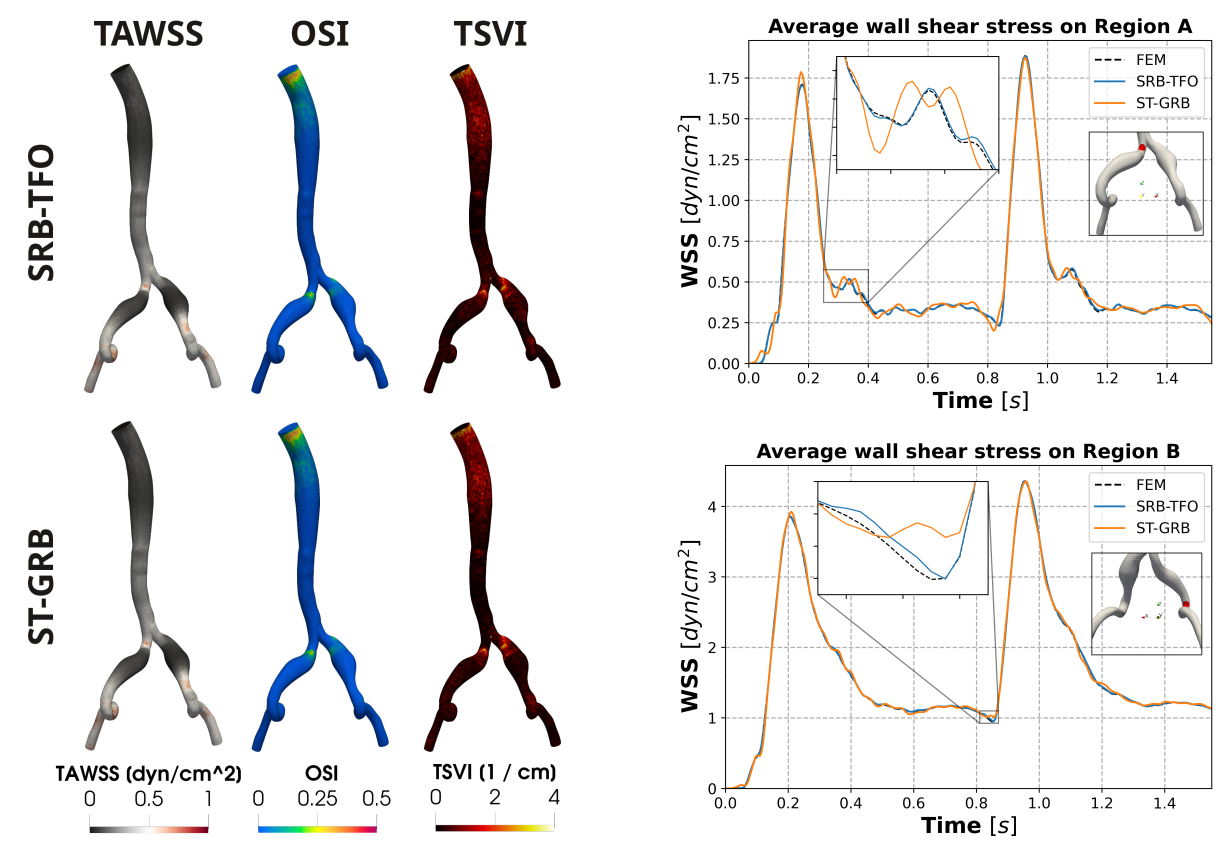


Figure 8. Wall shear stress approximation results, obtained with SRB–TFO and ST–GRB for $\varepsilon=10^{-3}$, $\mu_f^*=[0.11,13.2,2.40]$, $\mu_m^*=[0.097,1.50,3.07\cdot 10^6,0.43]$. In particular: (left) approximations of the time–averaged wall shear stress (TAWSS), oscillatory shear index (OSI) and topological shear variation index (TSVI); (right) trends over time of WSS, averaged in space over two different vessel wall portions, whose locations are depicted under the legend.

first application of ST-RB methods to reduced FSI models, particularly in the hæmodynamics context. The numerical results empirically demonstrated the ability of our model to quickly produce rather precise solution approximations. Nonetheless, we acknowledge that the classical RB method should be preferred over ST-GRB in high-precision applications or if the temporal dynamics arising within the high-fidelity solutions manifold are too complex. Indeed, the computational gains of ST-GRB over SRB-TFO vanish if the number of temporal modes is too large, compared to the number of discrete time instants.

Acknowledgements

This work was supported by the Swiss National Science Foundation (grant agreement No 200021_197021, "Datadriven approximation of hemodynamics by combined reduced order modeling and deep neural networks").

References

- [1] Erica L Schwarz, Luca Pegolotti, Martin R Pfaller, and Alison L Marsden. Beyond CFD: Emerging methodologies for predictive simulation in cardiovascular health and disease. *Biophysics Reviews*, 4(1), 2023.
- [2] Ivan Fumagalli, Stefano Pagani, Christian Vergara, Luca Dedé, Dilachew A Adebo, Maurizio Del Greco, Antonio Frontera, Giovanni Battista Luciani, Gianluca Pontone, Roberto Scrofani, and Alfio Quarteroni. The role of computational methods in cardiovascular medicine: a narrative review. *Translational Pediatrics*, 13(1), 2024. ISSN 2224-4344.

- [3] Casey M Fleeter, Gianluca Geraci, Daniele E Schiavazzi, Andrew M Kahn, and Alison L Marsden. Multilevel and multifidelity uncertainty quantification for cardiovascular hemodynamics. *Computer methods in applied mechanics and engineering*, 365:113030, 2020.
- [4] Yubing Shi, Patricia Lawford, and Rodney Hose. Review of 0–D and 1–D models of blood flow in the cardio-vascular system. *Biomedical engineering online*, 10:1–38, 2011.
- [5] Alfio Quarteroni, Andrea Manzoni, and Federico Negri. *Reduced basis methods for partial differential equations: an introduction*, volume 92. Springer, 2015.
- [6] Amirhossein Arzani and Scott TM Dawson. Data-driven cardiovascular flow modelling: examples and opportunities. *Journal of the Royal Society Interface*, 18(175):20200802, 2021.
- [7] Maziar Raissi, Paris Perdikaris, and George E Karniadakis. Physics—informed neural networks: A deep learning framework for solving forward and inverse problems involving nonlinear partial differential equations. *Journal of Computational physics*, 378:686–707, 2019.
- [8] Philipp Moser, Wolfgang Fenz, Stefan Thumfart, Isabell Ganitzer, and Michael Giretzlehner. Modeling of 3D blood flows with physics-informed neural networks: Comparison of network architectures. *Fluids*, 8(2):46, 2023.
- [9] Damiano Lombardi. Reduced order modelling for direct and inverse problems in haemodynamics. In *Reduced Order Models for the Biomechanics of Living Organs*, pages 235–253. Elsevier, 2023.
- [10] Jan S. Hesthaven, Cecilia Pagliantini, and Gianluigi Rozza. Reduced basis methods for time-dependent problems. Acta Numerica, 31:265–345, 2022.
- [11] Karsten Urban and Anthony T Patera. An improved error bound for reduced basis approximation of linear parabolic problems. *Mathematics of Computation*, 83(288):1599–1615, 2014.
- [12] Masayuki Yano. A space–time Petrov–Galerkin certified reduced basis method: application to the Boussinesq equations. *SIAM Journal on Scientific Computing*, 36(1):A232–A266, 2014.
- [13] Youngsoo Choi and Kevin Carlberg. Space–time least-squares Petrov–Galerkin projection for nonlinear model reduction. *SIAM Journal on Scientific Computing*, 41(1):A26–A58, 2019.
- [14] Y. S. Shimizu and E. J. Parish. Windowed space–time least–squares Petrov–Galerkin model order reduction for nonlinear dynamical systems. Computer Methods in Applied Mechanics and Engineering, 386:114050, 2021.
- [15] Y. Choi, P. Brown, W. Arrighi, R. Anderson, and K. Huynh. Space–time reduced order model for large–scale linear dynamical systems with application to Boltzmann transport problems. *Journal of Computational Physics*, 424, 2021.
- [16] Y. Kim, K. Wang, and Y. Choi. Efficient space–time reduced order model for linear dynamical systems in Python using less than 120 lines of code. *Mathematics* 2021, 9(14), 2021.
- [17] Riccardo Tenderini, Stefano Pagani, Alfio Quarteroni, and Simone Deparis. PDE–aware deep learning for inverse problems in cardiac electrophysiology. *SIAM Journal on Scientific Computing*, 44(3):B605–B639, 2022.
- [18] Riccardo Tenderini, Nicholas Mueller, and Simone Deparis. Space–time reduced basis methods for parametrized unsteady Stokes equations. *SIAM Journal on Scientific Computing*, 46(1):B1–B32, 2024.
- [19] Nicholas Mueller and Santiago Badia. Model order reduction with novel discrete empirical interpolation methods in space–time. *Journal of Computational and Applied Mathematics*, page 115767, 2024.
- [20] Fabio Nobile. Numerical approximation of fluid-structure interaction problems with application to hæmody-namics. PhD thesis, EPFL, Lausanne, 2001.
- [21] Philippe Moireau, Nan Xiao, Matteo Astorino, C Alberto Figueroa, Dominique Chapelle, Charles A Taylor, and J-F Gerbeau. External tissue support and fluid–structure simulation in blood flows. *Biomechanics and modeling in mechanobiology*, 11:1–18, 2012.
- [22] Ramón Pons, Andrea Guala, José F Rodríguez-Palomares, JC Cajas, Lydia Dux-Santoy, Gisela Teixidó-Tura, José Javier Molins, Mariano Vázquez, Arturo Evangelista, and Jordi Martorell. Fluid–structure interaction simulations outperform computational fluid dynamics in the description of thoracic aorta haemodynamics and in the differentiation of progressive dilation in Marfan syndrome patients. *Royal Society open science*, 7(2):191752, 2020.
- [23] Paolo Crosetto, Simone Deparis, Gilles Fourestey, and Alfio Quarteroni. Parallel algorithms for fluid–structure interaction problems in haemodynamics. *SIAM Journal on Scientific Computing*, 33(4):1598–1622, 2011.
- [24] Fabio Nobile, Matteo Pozzoli, and Christian Vergara. Time accurate partitioned algorithms for the solution of fluid–structure interaction problems in haemodynamics. *Computers & Fluids*, 86:470–482, 2013.

- [25] Santiago Badia, Fabio Nobile, and Christian Vergara. Robin–Robin preconditioned Krylov methods for fluid–structure interaction problems. Computer Methods in Applied Mechanics and Engineering, 198(33-36):2768–2784, 2009.
- [26] Simone Deparis, Davide Forti, Gwenol Grandperrin, and Alfio Quarteroni. FaCSI: A block parallel preconditioner for fluid–structure interaction in hemodynamics. *Journal of Computational Physics*, 327:700–718, 2016.
- [27] C Alberto Figueroa, Irene E Vignon-Clementel, Kenneth E Jansen, Thomas JR Hughes, and Charles A Taylor. A coupled momentum method for modeling blood flow in three-dimensional deformable arteries. *Computer methods in applied mechanics and engineering*, 195(41-43):5685–5706, 2006.
- [28] Claudia Maria Colciago, Simone Deparis, and Alfio Quarteroni. Comparisons between reduced order models and full 3D models for fluid–structure interaction problems in haemodynamics. *Journal of Computational and Applied Mathematics*, 265:120–138, 2014.
- [29] Claudia M Colciago and Simone Deparis. Reduced numerical approximation of reduced fluid–structure interaction problems with applications in haemodynamics. Frontiers in Applied Mathematics and Statistics, 4:18, 2018.
- [30] Luca Formaggia, Alfio Quarteroni, and Alessandro Veneziani. *Cardiovascular Mathematics: modeling and simulation of the circulatory system*, volume 1. Springer Science & Business Media, 2010.
- [31] C Alberto Figueroa, Charles A Taylor, Victoria Yeh, Allen J Chiou, and Christopher K Zarins. Effect of curvature on displacement forces acting on aortic endografts: a 3–dimensional computational analysis. *Journal of Endovascular Therapy*, 16(3):284–294, 2009.
- [32] A Cristiano I Malossi, Pablo J Blanco, and Simone Deparis. A two–level time step technique for the partitioned solution of one–dimensional arterial networks. *Computer Methods in Applied Mechanics and Engineering*, 237: 212–226, 2012.
- [33] Yi Liu, Charles Dang, Marisa Garcia, Hans Gregersen, and Ghassan S Kassab. Surrounding tissues affect the passive mechanics of the vessel wall: theory and experiment. *American Journal of Physiology-Heart and Circulatory Physiology*, 293(6):H3290–H3300, 2007.
- [34] Franco Brezzi. On the existence, uniqueness and approximation of saddle–point problems arising from Lagrangian multipliers. *Publications mathématiques et informatique de Rennes*, (S4):1–26, 1974.
- [35] Daniele Boffi, Franco Brezzi, Michel Fortin, et al. *Mixed finite element methods and applications*, volume 44. Springer, 2013.
- [36] Luca Pegolotti, Martin R Pfaller, Alison L Marsden, and Simone Deparis. Model order reduction of flow based on a modular geometrical approximation of blood vessels. *Computer methods in applied mechanics and engineering*, 380:113762, 2021.
- [37] Nathan Halko, Per-Gunnar Martinsson, and Joel A Tropp. Finding structure with randomness: probabilistic algorithms for constructing approximate matrix decompositions. *SIAM review*, 53(2):217–288, 2011.
- [38] Gianluigi Rozza. On optimization, control and shape design of an arterial bypass. *International Journal for Numerical Methods in Fluids*, 47(10-11):1411–1419, 2005.
- [39] Saifon Chaturantabut and Danny C Sorensen. Nonlinear model reduction via discrete empirical interpolation. *SIAM Journal on Scientific Computing*, 32(5):2737–2764, 2010.
- [40] Daniel Wirtz, Danny C Sorensen, and Bernard Haasdonk. A posteriori error estimation for DEIM reduced nonlinear dynamical systems. *SIAM Journal on Scientific Computing*, 36(2):A311–A338, 2014.
- [41] Margarita Chasapi, Pablo Antolin, and Annalisa Buffa. A localized reduced basis approach for unfitted domain methods on parameterized geometries. Computer Methods in Applied Mechanics and Engineering, 410:115997, 2023.
- [42] Kevin Carlberg, Jaideep Ray, and Bart van Bloemen Waanders. Decreasing the temporal complexity for nonlinear, implicit reduced—order models by forecasting. *Computer Methods in Applied Mechanics and Engineering*, 289:79–103, 2015.
- [43] Tan Bui-Thanh, Murali Damodaran, and Karen Willcox. Aerodynamic data reconstruction and inverse design using proper orthogonal decomposition. *AIAA journal*, 42(8):1505–1516, 2004.
- [44] Michele Girfoglio, Francesco Ballarin, Giuseppe Infantino, Francesca Nicoló, Andrea Montalto, Gianluigi Rozza, Roberto Scrofani, Marina Comisso, and Francesco Musumeci. Non-intrusive PODI–ROM for patient-specific aortic blood flow in presence of a LVAD device. *Medical Engineering & Physics*, 107:103849, 2022.
- [45] Nathan M Wilson, Ana K Ortiz, and Allison B Johnson. The vascular model repository: a public resource of medical imaging data and blood flow simulation results. *Journal of medical devices*, 7(4):040923, 2013.

- [46] Luca Bertagna, Simone Deparis, Luca Formaggia, Davide Forti, and Alessandro Veneziani. The LifeV library: engineering mathematics beyond the proof of concept. *arXiv preprint arXiv:1710.06596*, 2017.
- [47] Youcef Saad and Martin H Schultz. GMRES: a generalized minimal residual algorithm for solving nonsymmetric linear systems. *SIAM Journal on scientific and statistical computing*, 7(3):856–869, 1986.
- [48] A Cristiano I Malossi and Jean Bonnemain. Numerical comparison and calibration of geometrical multiscale models for the simulation of arterial flows. *Cardiovascular Engineering and Technology*, 4:440–463, 2013.
- [49] Adam Updegrove, Nathan M Wilson, Jameson Merkow, Hongzhi Lan, Alison L Marsden, and Shawn C Shadden. SimVascular: an open source pipeline for cardiovascular simulation. *Annals of biomedical engineering*, 45:525–541, 2017.
- [50] David N Ku, Don P Giddens, Christopher K Zarins, and Seymour Glagov. Pulsatile flow and atherosclerosis in the human carotid bifurcation. Positive correlation between plaque location and low oscillating shear stress. *Arteriosclerosis: An Official Journal of the American Heart Association, Inc.*, 5(3):293–302, 1985.
- [51] Giuseppe De Nisco, Paola Tasso, Karol Calò, Valentina Mazzi, Diego Gallo, Francesca Condemi, Solmaz Farzaneh, Stéphane Avril, and Umberto Morbiducci. Deciphering ascending thoracic aortic aneurysm hemodynamics in relation to biomechanical properties. *Medical engineering & physics*, 82:119–129, 2020.
- [52] Valentina Mazzi, Giuseppe De Nisco, Ayla Hoogendoorn, Karol Calò, Claudio Chiastra, Diego Gallo, David A Steinman, Jolanda J Wentzel, and Umberto Morbiducci. Early atherosclerotic changes in coronary arteries are associated with endothelium shear stress contraction/expansion variability. *Annals of Biomedical Engineering*, 49:2606–2621, 2021.
- [53] Arnav Kumar, Elizabeth W Thompson, Adrien Lefieux, David S Molony, Emily L Davis, Nikita Chand, Stephane Fournier, Hee Su Lee, Jon Suh, Kimi Sato, et al. High coronary shear stress in patients with coronary artery disease predicts myocardial infarction. *Journal of the American College of Cardiology*, 72(16):1926–1935, 2018.
- [54] Alessandro Candreva, Mattia Pagnoni, Maurizio Lodi Rizzini, Takuya Mizukami, Emanuele Gallinoro, Valentina Mazzi, Diego Gallo, David Meier, Toshiro Shinke, Jean-Paul Aben, et al. Risk of myocardial infarction based on endothelial shear stress analysis using coronary angiography. *Atherosclerosis*, 342:28–35, 2022.
- [55] Parastou Eslami, Justin Tran, Zexi Jin, Julia Karady, Romina Sotoodeh, Michael T Lu, Udo Hoffmann, and Alison Marsden. Effect of wall elasticity on hemodynamics and wall shear stress in patient–specific simulations in the coronary arteries. *Journal of biomechanical engineering*, 142(2):024503, 2020.

A ST-GRB problem with inhomogeneous initial conditions

In this section, we extend the ST-RB problem formulation presented in Section 3.2 by considering non-zero initial conditions for both the velocity and the displacement field. To this aim, we introduce the set of vectors $U_0 := \{u_{1-s}\}_{s=1}^S \in \mathbb{R}^{N_u^s}$, that contains the initial conditions for the velocity field at the S discrete time instants $\{(1-s)\Delta t\}_{s=1}^S$. Analogously, we define $D_0 := \{d_{1-s}\}_{s=1}^S \in \mathbb{R}^{N_d^s}$ as the set of initial conditions for the displacement field. Incidentally, we underline that, for simplicity, we suppose to know velocity and displacement not just at t=0, but also at S-1 previous time instants.

Compared to Eq.(2.5), the right-hand side vector in the full-order algebraic system now features a non-zero velocity block, that accounts for enforcing the velocity initial conditions. Specifically, such term is of the form $F_1^{st}(U_0) + F_1^{\Gamma,st}(\tilde{\mu}_m, U_0)$, where

$$\begin{aligned} \boldsymbol{F}_{1}^{st}(\boldsymbol{U_{0}}) &= \left[\left(\sum_{s=1}^{S} \alpha_{s} \boldsymbol{M} \boldsymbol{u}_{1-s} \right)^{T}, \; \cdots, \left(\sum_{s=S}^{S} \alpha_{s} \boldsymbol{M} \boldsymbol{u}_{S-s} \right)^{T}, \; \underbrace{\left(\boldsymbol{0}_{N_{u}^{s}} \right)^{T}, \; \cdots, \; \left(\boldsymbol{0}_{N_{u}^{s}} \right)^{T}}_{N^{t}-S} \right]^{T}; \\ \boldsymbol{F}_{1}^{\Gamma,st}(\tilde{\boldsymbol{\mu}}_{\boldsymbol{m}}, \boldsymbol{U_{0}}) &= \left[\left(\sum_{s=1}^{S} \alpha_{s} (\tilde{\boldsymbol{\mu}}_{\boldsymbol{m}})_{1} \; \boldsymbol{M}_{\boldsymbol{s}} \right) \boldsymbol{u}_{1-s}^{T}, \; \cdots, \; \left(\sum_{s=S}^{S} \alpha_{s} (\tilde{\boldsymbol{\mu}}_{\boldsymbol{m}})_{1} \; \boldsymbol{M}_{\boldsymbol{s}} \boldsymbol{u}_{S-s} \right)^{T}, \; \underbrace{\left(\boldsymbol{0}_{N_{u}^{s}} \right)^{T}, \; \cdots, \left(\boldsymbol{0}_{N_{u}^{s}} \right)^{T}}_{N^{t}-S} \right]^{T}. \end{aligned}$$

Within the ST-RB formulation, these two contributions translate into two non-zero velocity right-hand side blocks of the form

$$\begin{split} \widehat{F}_1\big(\boldsymbol{U_0}\big) &= \left(\boldsymbol{\Pi}^u\right)^T \boldsymbol{F}_1^{st}\big(\boldsymbol{U_0}\big) \in \mathbb{R}^{n_u^{st}} \qquad \text{where} \quad \left(\widehat{F}_1\right)_{\ell} = \sum_{s=1}^S \sum_{s'=s}^S \alpha_{s'} \left(\overline{\boldsymbol{M}} \overline{\boldsymbol{u}}_{s-s'}\right)_{\ell_s} \left(\psi_{\ell_t}^u\right)_s \; ; \\ \widehat{F}_1^{\Gamma}\big(\tilde{\boldsymbol{\mu}}_{\boldsymbol{m}}, \boldsymbol{U_0}\big) &= \left(\boldsymbol{\Pi}^u\right)^T \boldsymbol{F}_1^{\Gamma,st}\big(\tilde{\boldsymbol{\mu}}_{\boldsymbol{m}}, \boldsymbol{U_0}\big) \in \mathbb{R}^{n_u^{st}} \qquad \text{where} \quad \left(\widehat{F}_1^{\Gamma}\big(\tilde{\boldsymbol{\mu}}_{\boldsymbol{m}}\big)\right)_{\ell} = (\tilde{\boldsymbol{\mu}}_{\boldsymbol{m}})_1 \sum_{s=1}^S \sum_{s'=s}^S \alpha_{s'} \left(\overline{\boldsymbol{M}}_s \overline{\boldsymbol{u}}_{s-s'}\right)_{\ell_s} \left(\psi_{\ell_t}^u\right)_s \; . \end{split}$$

To account for inhomogeneous initial conditions on the displacement field, we need to include an additional term $d_0^{st} \in \mathbb{R}^{N_u^{st}}$ in Eq.(3.1). In particular, the spatio-temporal displacement is now approximated as

$$\boldsymbol{d}^{st} \approx \sum_{\ell=1}^{n_u^{st}} \widehat{\boldsymbol{u}}_{\ell} \boldsymbol{\pi}_{\ell}^d + \boldsymbol{d}_0^{st} = \sum_{\ell=1}^{n_u^{st}} \widehat{\boldsymbol{u}}_{\ell} \left(\boldsymbol{\varphi}_{\ell_s}^u \otimes \mathcal{P}_0 \left(\mathcal{E}_S^t \left(\boldsymbol{\psi}_{\ell_t}^u \right) \right) \right) + \sum_{\ell_0 = 1 - S}^{0} \boldsymbol{d}_{\ell_o} \otimes \left(\boldsymbol{\psi}_{\ell_0}^d \right)_{S:} , \tag{A.1}$$

where the subscript notation $(\cdot)_{S}$: indicates that the first S entries of $\{\varphi_{\ell_0}^d\}_{\ell_0=1-S}^0$ are discarded. The term d_0^{st} comprises the sum of S terms — since we employ a S-steps multistep scheme — and it is constructed through the use of "auxiliary" temporal modes $\psi_{\ell_0}^d \in \mathbb{R}^{N^t+S}$, with $\ell_0 \in \{1-S, \cdots, 0\}$. The latter are defined so that the numerical approximation of the first derivative in time of d_0^{st} is equal to zero at all the discrete time instants, namely we have

$$\psi_{\ell_0}^d \in \mathbb{R}^{N^t + S}: \quad \left(\psi_{\ell_0}^d\right)_n = \begin{cases} 1 & \text{if } n = \ell_0 \ ; \\ 0 & \text{if } 1 - S \le n \le 0, \ n \ne \ell_0 \ ; \\ \sum_{s=1}^S \alpha_s \left(\psi_{\ell_0}^d\right)_{n-s} & \text{if } 1 \le n \le N^t \ . \end{cases}$$

In this way, we can enforce non-zero initial conditions on the displacement without affecting its kinematic coupling with the velocity.

The use of Eq.(A.1) entails the presence of an additional right-hand contribution $F_{1,d}^{\Gamma,st}(\tilde{\mu}_m,D_0) \in \mathbb{R}^{N_u^{st}}$ in the full-order velocity right-hand side vector block. Specifically, we have

$$F_{1,d}^{\Gamma,st}(\tilde{\boldsymbol{\mu}}_{\boldsymbol{m}},\boldsymbol{D_0}) = -\sum_{\ell_0=1-S}^{0} \left(\left(\sum_{q=1}^{2} (\tilde{\boldsymbol{\mu}}_{\boldsymbol{m}})_{q+1} \boldsymbol{A}_{\boldsymbol{s}}^{q} + \beta \Delta t \ c_s \boldsymbol{M_s} \right) \boldsymbol{d}_{\ell_0} \right) \otimes (\boldsymbol{\psi}_{\ell_0}^{d}) \ .$$

In the ST-RB problem, this results in the presence of a new parameter-dependent right-hand side velocity block $\widehat{F}_{1.d}^{\Gamma}(\tilde{\mu}_m) \in \mathbb{R}^{n_u^{st}}$, whose entries read as

$$\left(\widehat{\boldsymbol{F}}_{1,d}^{\Gamma}(\widetilde{\boldsymbol{\mu}}_{\boldsymbol{m}})\right)_{\ell} = -\sum_{\ell_0=1-S}^{0} \left(\left(\sum_{q=1}^{2} (\widetilde{\boldsymbol{\mu}}_{\boldsymbol{m}})_{q+1} \overline{\boldsymbol{A}}_{\boldsymbol{s}}^{q} + \beta \Delta t \ c_s \overline{\boldsymbol{M}}_{\boldsymbol{s}} \right) \overline{\boldsymbol{d}}_{\ell_0} \right)_{\ell_s} \left((\boldsymbol{\psi}_{\ell_t}^u)^T (\boldsymbol{\psi}_{\ell_0}^d)_{S:} \right).$$

Ultimately, the incorporation of inhomogeneous initial conditions o velocity and displacement modifies the expression of the space–time–reduced residual $\hat{r}(\hat{w})$ as follows:

$$\widehat{\boldsymbol{r}}(\widehat{\boldsymbol{w}}) = \widehat{\boldsymbol{F}}(\boldsymbol{\mu_f}) + \widehat{\mathcal{E}}_u \big(\widehat{\boldsymbol{F}}_1(\boldsymbol{U_0}) + \widehat{\boldsymbol{F}}_1^{\Gamma}(\tilde{\boldsymbol{\mu}_m}, \boldsymbol{U_0}) + \widehat{\boldsymbol{F}}_{1,d}^{\Gamma}(\tilde{\boldsymbol{\mu}_m}, \boldsymbol{D_0}) \big) - \Big(\widehat{\boldsymbol{A}} + \widehat{\boldsymbol{A}}^{\Gamma}(\tilde{\boldsymbol{\mu}_m})\Big) \, \widehat{\boldsymbol{w}} - \widehat{\mathcal{E}}_u \big(\widehat{\boldsymbol{c}}(\widehat{\boldsymbol{u}})\big) - \widehat{\mathcal{E}}_u \big((\widehat{\boldsymbol{A}}_s(\tilde{\boldsymbol{\mu}_m}) + \widehat{\boldsymbol{E}}_s) \, \widehat{\boldsymbol{u}}\big) \, ,$$

where $\widehat{\mathcal{E}}_u: \mathbb{R}^{n_u^{st}} \to \mathbb{R}^{n^{st}}$ is space–time–reduced velocity zero–padding operator, introduced in Eq.(3.7a).